Correspondence to:
M. J. Coleman,
colemanmarco@gmail.com

Lateral Termination of a Cycladic-Style Detachment System (Hymittos, Greece)

M. J. Coleman[1] (ID), **D. A. Schneider[1]** (ID), **B. Grasemann[2]** (ID), **K. Soukis[3]** (ID), **S. Lozios[3]**, and **M. S. Hollinetz[2]** (ID)

[1]Department of Earth and Environmental Science, University of Ottawa, Ottawa, Ontario, Canada, [2]Department of Geodynamics and Sedimentology, University of Vienna, Vienna, Austria, [3]Department of Geology and Geoenvironment, National and Kapodistrian University of Athens, Athens, Greece

Abstract The bedrock of Hymittos, Attic peninsula, Greece, exposes a pair of low-angle crustal-scale ductile-then-brittle detachment faults. The uppermost detachment fault separates sub-greenschist facies phyllite and marble of a Pelagonian Zone hanging wall, from greenschist facies metasedimentary schist, calc-schist, and marble correlated to the Cycladic Blueschist Unit. A second, structurally lower detachment fault subdivides the metamorphic rocks of the Cycladic blueschist unit footwall into middle and lower units. There is a marked step in metamorphic grade between the sub-greenschist facies uppermost package, and the middle-to-upper greenschist facies middle and lower packages. A suite of new white mica $^{40}Ar/^{39}Ar$ and zircon (U-Th)/He dates indicates accommodation of deformation along these faults occurred from the late Oligocene to the late Miocene with both faults active during the middle Miocene. The structures have clear top-S/SSW kinematics determined from flanking folds, sigmoids, shear bands, stair-stepping of strain shadows on porphyroclasts, and SCC′ fabrics. The ductile-to-brittle deformation of the structures, morphology of the massif, and the increase in metamorphic grade suggest these low-angle structures are part of a major, crustal-scale extensional complex, located at the northwest end of the West Cycladic Detachment System, that accommodated Miocene bivergent exhumation of Attic-Cycladic metamorphic core complexes in the central Aegean. Taken together, the above data suggest that multiple coeval detachment branches may form in areas with high strain gradients to accommodate the mechanically necessary termination of Cycladic-style detachment systems.

1. Introduction

In the Aegean Sea, high-pressure metamorphic rocks of the Attic-Cycladic Complex (ACC) have been exhumed along crustal-scale extensional detachment faults as a series of asymmetric metamorphic core complexes (Figure 1; Lister et al., 1984; Jolivet & Brun, 2010; Grasemann et al., 2012). Four major low-angle detachment systems have been identified accommodating the bivergent extension of the ACC: (1) the top-NNE North Cycladic detachment system (NCDS) is exposed on Andros, Tinos, Mykonos, and Ikaria (Beaudoin et al., 2015; Jolivet et al., 2010); (2) the top-SSW West Cycladic detachment system (WCDS) exposed on Attica, Kea, Kythnos, Serifos, with a brittle manifestation on Sifnos and Folegandros (Augier et al., 2015; Coleman et al., 2019; Grasemann et al., 2012; Iglseder et al., 2011; Lekkas et al., 2011; Roche et al., 2016); (3) the top-N Naxos-Paros detachment system (NPD) exhumes amphibolite and granulite facies marble, gneiss and migmatite (Urai et al., 1990); and (4) the top-S Santorini detachment (SD; Schneider et al., 2018; Figure 1). Where syn-tectonic plutonism is absent, detachments are commonly a single cataclastic to brittle fault plane and a broad zone of penetrative, ductile deformation extends hundreds of meters into the footwall (Grasemann et al., 2012; Iglseder et al., 2011). In contrast, the effects of plutonism apparently generates multiple detachment fault planes that diachronously localize deformation (Rabillard et al., 2015, 2018).

Extensional detachments are useful natural laboratories for studying fault processes that accommodate exhumation, as displacement along a low-angle normal fault exhumes footwall rocks. Typically, the center of a fault (lengthwise) exhibits the maximum displacement, with zero displacement at each of the fault terminations (Elliott, 1976). The ends of faults are often characterized by damage zones produced by the concentration of stress resulting in secondary faults or fractures mechanically linked to the main fault (Cowie & Scholz, 1992; Martel, 1997). The faults or fractures accommodating this stress often occur as a characteristic
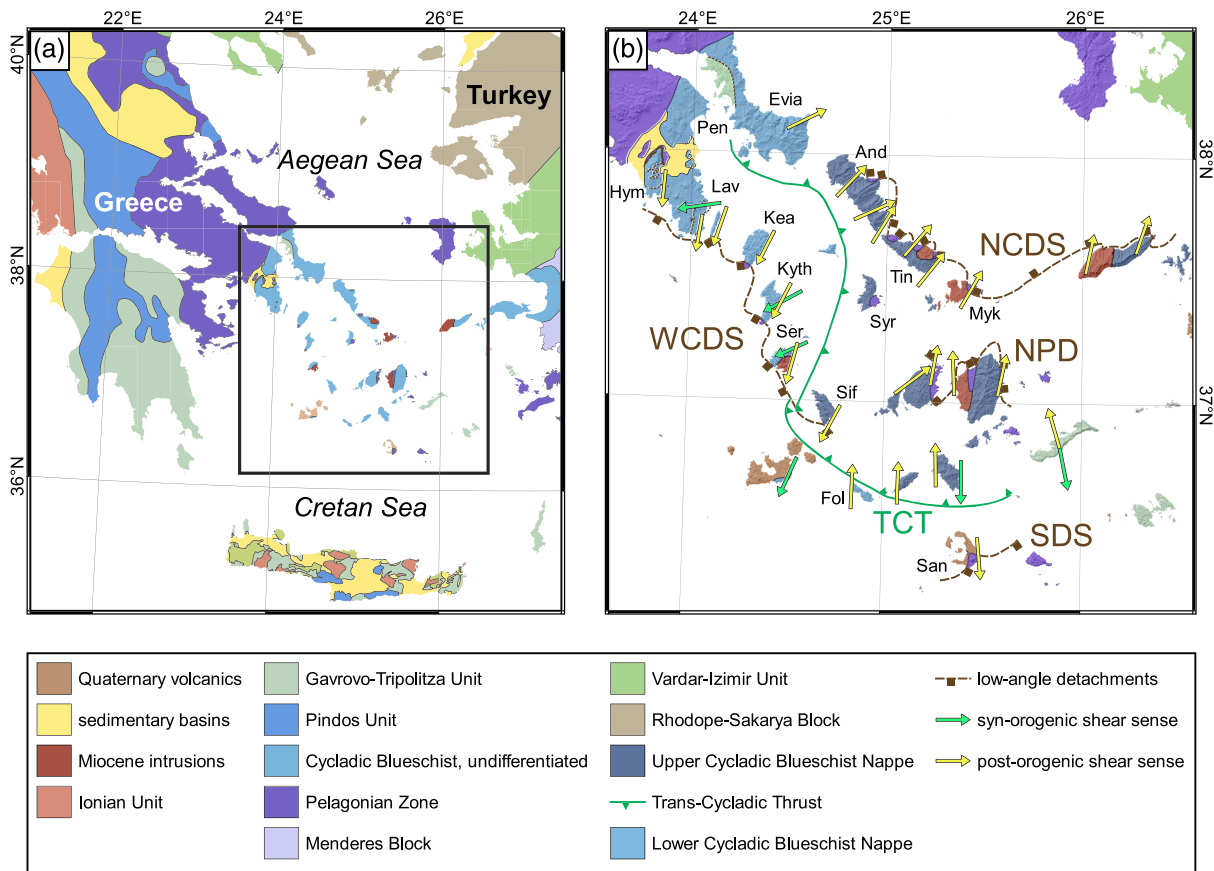
Figure 1. (a) Simplified bedrock geological map of the Hellenides in Greece, Turkey, and Crete as well as the Aegean and Cretan seas. The Hellenides are a series of nappes recording the accretion of oceanic basins and microcontinents to the European continental margin. (b) Simplified bedrock geological map of Greece and the central Aegean. Post-orogenic, Oligo-Miocene low-angle extensional detachments include the top-SSW West Cycladic Detachment System (WCDS; Grasemann et al., 2012), the top-NE North Cycladic Detachment System (NCDS; Jolivet et al., 2010), the top-NE Naxos-Paros Detachment (NPD; Urai et al., 1990; Buick, 1991), and the top-SSE Santorini Detachment System (SDS; Schneider et al., 2018). The Lower and Upper Cycladic Blueschist Nappes (LCBN and UCBN) are subdivisions of the Cycladic Blueschist Unit; separated by the Eocene Trans-Cycladic Thrust (TCT; Grasemann et al., 2018). The Pelagonian Zone is the amphibolite facies to unmetamorphosed hanging wall of the Cycladic detachment systems. Post-orogenic shear sense indicates the directions of displacement along the low-angle detachment systems accommodating bivergent extension and exhumation of the Cycladic Blueschist Unit (Augier et al., 2015; Beaudoin et al., 2015; Brichau et al., 2007; Faure et al., 1991; Forster & Lister, 1999; Gautier & Brun, 1994; Grasemann et al., 2012; Huet et al., 2009; Jolivet et al., 2010; Jolivet & Patriat, 1999; Laurent et al., 2016; Lister et al., 1984; Mehl et al., 2005, 2007; Ring et al., 2011; Soukis & Stockli, 2013). Hym: Hymittos, Pen: Pentelli, Lav: Lavrion, Kyth: Kythnos, Ser: Serifos, Sif: Sifnos, Syr: Syros, And: Andros, Tin: Tinos, Myk: Mykonos, San: Santorini, Fol: Folegandros. The map is projected in the geographic coordinate system, using the World Geodetic System (WGS) 1984 datum.

structure or combination of structures including wing cracks, horsetails, synthetic branch faults, and antithetic faults (Kim & Sanderson, 2006). Although, the mechanics of the growth of normal faults considering multilayers have been studied in detail (Schöpfer et al., 2017, and references therein), the structural complexity at the termination of crustal scale detachments systems, which may reactivate earlier nappe stacks, is less well understood.

The relatively understudied bedrock of Hymittos Mountain on the Attic Peninsula of Greece offers an excellent opportunity to study the northwestern termination of the WCDS. The local tectonostratigraphy is characterized by three tectonic packages consisting of variably intercalated phyllites, marbles and schists, divided by a pair of low-angle, crustal-scale detachment faults. Similarities in lithologies, metamorphic grades, structural styles and kinematics, and geomorphology suggest that these rocks expose a metamorphic core complex of the ACC. Bedrock mapping, white mica ^{40}Ar/^{39}Ar and zircon (U-Th)/He ages, and petrographic and structural analysis suggest these faults are the northernmost exposure of the WCDS (Figure 1b), and their geodynamic position suggests it must be very close to the detachment systems terminus. Unlike elsewhere in the western Cyclades, the hanging wall is quite well preserved, and

its ophiolitic and marble sequences are correlated to the Pelagonian Zone, and the lower two packages are likely equivalents of the high-pressure Cycladic Blueschist Unit. The new low-temperature geochronology indicates the detachment faults of the massif were coeval, possibly suggesting a third type of Cycladic-style detachment system.

2. Geological Setting

2.1. Geodynamic Evolution of the Central Aegean

In the central Mediterranean, Late Jurassic to Cenozoic north-directed convergence at the Eurasian continental margin led to subduction of the Apulian microcontinent and accretion of numerous exotic terranes, building a nappe stack termed the Hellenides (Jacobshagen, 1986; Ring et al., 2010). The nappes comprising the Hellenides are the Pelagonian, Pindos, Gavrovo-Tripolitza, Phyllite-Quartzite, Ionian, and pre-Apulian thrust units (Figure 1a; Jolivet & Brun, 2010). The majority of central Aegean bedrock is correlated to the Cycladic Blueschist (proposed to be metamorphosed Pindos; e.g., Papanikolaou, 1984, 1987, 2009) and Pelagonian units. Within the Mediterranean, the Aegean Sea is one of a series of Cenozoic back-arc basins distributed along the Europe-Africa continental margin. The opening of the Aegean initiated ca. 35 Ma as a result of slab rollback and subsequent back-arc spreading (Jolivet & Faccenna, 2000; Royden, 1993). Extension began in the northern Aegean and migrated southwards through time (Fytikas et al., 1984; Jolivet et al., 2003). In the southern Aegean, extension was accompanied by greenschist facies deformation that overprinted Eocene-Oligocene high-pressure assemblages as a series of bivergent NNE-SSW oriented metamorphic core complexes (MCCs) (Figure 1b; Grasemann et al., 2012; Jolivet & Brun, 2010; Lister et al., 1984).

The Pelagonian Zone is the remnants of a subducted microcontinent consisting of Paleozoic basement with a Paleozoic-Mesozoic carbonate cover, overlain by a Triassic-Jurassic ophiolite, Cretaceous carbonates and a Paleocene-Eocene flysch (Aubouin, 1959; Bonneau, 1984; Bonneau & Kienast, 1982; Jacobshagen, 1986). The package of rocks comprises the hanging wall of the Cycladic detachments on the islands, where it occurs as isolated klippen of metasedimentary, metabasic, and ophiolitic rocks frequently of low metamorphic grade (Coleman et al., 2019; Grasemann et al., 2012; Schneider et al., 2018). Higher-grade Pelagonian metamorphic rocks within the Cyclades record middle Cretaceous high-pressure, Late Cretaceous greenschist to amphibolite facies metamorphism (Altherr et al., 1994; Bonneau, 1984; Huet et al., 2014; Reinecke et al., 1982), equivalent to exposures of the Pelagonian Zone on Evia (Maluski et al., 1981) and the Greek mainland (Lips et al., 1998) (Altherr et al., 1994; Dürr et al., 1978; Maluski et al., 1987; Patzak et al., 1994; Reinecke et al., 1982; Schermer et al., 1990). Pelagonian Zone rocks were thrust atop the Pindos Unit during 55–30 Ma subduction and accretion at the European continental margin (Skourlis & Doutsos, 2003). The rocks of the Pindos Unit are Late Triassic to Paleocene pelagic limestones and siliciclastic rocks, overlain by a Maastrichtian-Eocene flysch sequence (Aubouin, 1959; Brunn, 1956; Stampfli et al., 2003).

The Cycladic Blueschist Unit (CBU) is the proposed paleogeographic equivalent of the Pindos Unit in the Cyclades (Bonneau, 1984; Bonneau & Kienast, 1982). Other proposed correlations include a Vardar affinity (Chatzaras et al., 2013; Doutsos et al., 1993), possibly deposited in a rift-basin within or northeast of the Pelagonian Zone (Zlatkin et al., 2018). Some authors suggest that the proto-CBU formed as a Late Cretaceous back-arc basin above the subducting Pindos Ocean (Keiter et al., 2011); others suggest CBU is the southernmost margin of the Pelagonian microcontinent (Bonneau, 1984). Regardless of affinity, the CBU consists of a Permo-Carboniferous to latest Cretaceous passive margin marble, metapelite, and metavolcanic sequence (Dürr et al., 1978; Poulaki et al., 2019). Polyphase deformation and metamorphism have reworked the original CBU stratigraphy (Brun & Faccenna, 2008; Jolivet et al., 2003). The CBU experienced Eocene high-pressure metamorphism during collision and subduction of the Pindos ocean basin (Altherr et al., 1979; Okrusch & Bröcker, 1990; Tomaschek et al., 2003). Zircon U-Pb, white mica ^{40}Ar/^{39}Ar, and garnet Sm-Nd and Lu-Hf ages suggest peak eclogite to blueschist facies metamorphism occurred at 52 Ma continuing until 40 Ma (Dragovic et al., 2015; Forster & Lister, 2005; Lagos et al., 2007; Laurent et al., 2017; Ring & Layer, 2003; Schneider et al., 2011; Tomaschek et al., 2003). The Cycladic Blueschist Unit overlies the Cycladic Basement unit, which is a polymetamorphic terrane comprising Pre-Carboniferous schists intruded by Carboniferous granitic rocks (Flansburg et al., 2019; Reischmann, 1998).

A ca. 40–30 Ma Eocene-Oligocene metamorphic event linked to synorogenic exhumation driven by ductile extrusion has been identified by white mica $^{40}Ar/^{39}Ar$ and Rb-Sr dating (Gerogiannis et al., 2019; Huet et al., 2009; Jolivet et al., 2010; Ring et al., 2007; Scheffer et al., 2016; Schneider et al., 2011). Deeper levels of the CBU are suggested to have continued experiencing high-pressure metamorphism until 30 Ma (Huet et al., 2014; Lister & Forster, 2016; Wijbrans et al., 1990) even as the higher structural levels were partially exhumed and undergoing contemporaneous greenschist facies metamorphism (Ring et al., 2010). Other authors consider this an entirely greenschist facies metamorphic event (Cao et al., 2018). The CBU has been subdivided into the eclogite facies Upper (UCBN) and blueschist facies Lower Cycladic Blueschist nappes (LCBN), separated by the synorogenic Trans-Cycladic Thrust (Figure 1b; Grasemann et al., 2018; Wind et al., 2020).

Subsequent post-orogenic slab rollback during the Oligo-Miocene drove back-arc extension leading to diachronous 25–18 Ma greenschist facies metamorphism (Altherr et al., 1982; Bröcker et al., 2004; Cossette et al., 2015; Iglseder et al., 2011; Parra et al., 2002; Wijbrans & McDougall, 1986, 1988) and exhumation of Attic-Cycladic metamorphic core complexes along a series of low-angle extensional detachment faults (Jolivet & Brun, 2010; Lister et al., 1984).

Cycladic detachments are frequently associated with I- and/or S-type granitoids (i.e., Serifos, Ikaria, Naxos, and Paros; Figure 1b). Magmatism has migrated from the northeast to the southwest in the Aegean and is associated with slab-tearing and clockwise rotation of the External Hellenides (Jolivet et al., 2015). Where detachments exhibit a spatial relationship with these granitoids, deformation was frequently accommodated by multi-plane detachment systems (Beaudoin et al., 2015; Brichau et al., 2010; Iglseder et al., 2009; Serifos, Tinos, Mykonos, Ikaria; Grasemann & Petrakakis, 2007; Tschegg & Grasemann, 2009). The multiple detachment branches are suggested to be produced by stalling of the rising granitic melt at the brittle-ductile transition (Rabillard et al., 2018). Cooling of the granitoid inhibited deformation along a structurally lower detachment; simultaneously, thermal weakening of the crust above the pluton led to initiation of a new, structurally higher detachment producing a multi-plane detachment system. On Cycladic islands where plutons are not observed, detachments frequently are a single fault plane with a zone of diffuse ductile deformation extending several hundreds of meters below the detachment core (e.g., Grasemann et al., 2012; Kea, Kythnos; Iglseder et al., 2011).

2.2. Regional Geology of the Attic Peninsula

The tectonostratigraphy and structural style of the western Cycladic islands can be extended to the Lavrion District, southern Attic peninsula (Berger et al., 2013; Katsiavrias et al., 1991; Krohe et al., 2010; Lekkas & Lozios, 2000; Lekkas et al., 2011; Leleu & Neumann, 1969; Marinos & Petraschek, 1956; Papanikolaou, Bassi, et al., 2004; Papanikolaou, Lozios, et al., 2004; Photiades & Carras, 2001; Photiades & Saccani, 2006; Scheffer et al., 2016; Seman et al., 2017). The bedrock of Lavrion exposes a tripartite tectonostratigraphy separated by a pair of top-SSW low-angle detachments correlated to the WCDS (Coleman et al., 2019; Lekkas et al., 2011; Scheffer et al., 2016). The upper tectonic unit of Lavrion is correlated to the Pelagonian Zone; the middle and lower tectonostratigraphic units have been correlated to the LCBN (Coleman et al., 2019; Scheffer et al., 2016).

The provenance of rocks exposed on the western Attic Peninsula including Hymittos and Penteli Mountains is still under debate. Some authors suggest the crystalline rocks are extensions of the ACC (Diamantopoulos et al., 2009; Krohe et al., 2010), yet others infer these rocks to be exposures of the Gavrovo-Tripolitza Unit (Ring et al., 2010), or the Cycladic Basal Unit (Baziotis & Mposkos, 2011; Baziotis et al., 2009; Liati et al., 2013). Similarly, the nature of the major tectonic boundary separating crystalline rocks from the hanging wall is not yet clarified; previous investigations interpreted the boundary as an Alpine thrust or a transpressional fault (Clement, 1976; Marinos & Petraschek, 1956; Papanikolaou & Papanikolaou, 2007; Papanikolaou & Royden, 2007; Xypolias et al., 2003) whereas other authors interpreted Hymittos and Penteli mountains as a series of asymmetric metamorphic core complexes formed by NNW-directed extensional faulting (Diamantopoulos et al., 2009). Penteli has also been interpreted as an isoclinally folded stratigraphy correlative to that of the middle and lower units of Lavrion, though metamorphosed under different P-T conditions (Lozios et al., 2019).
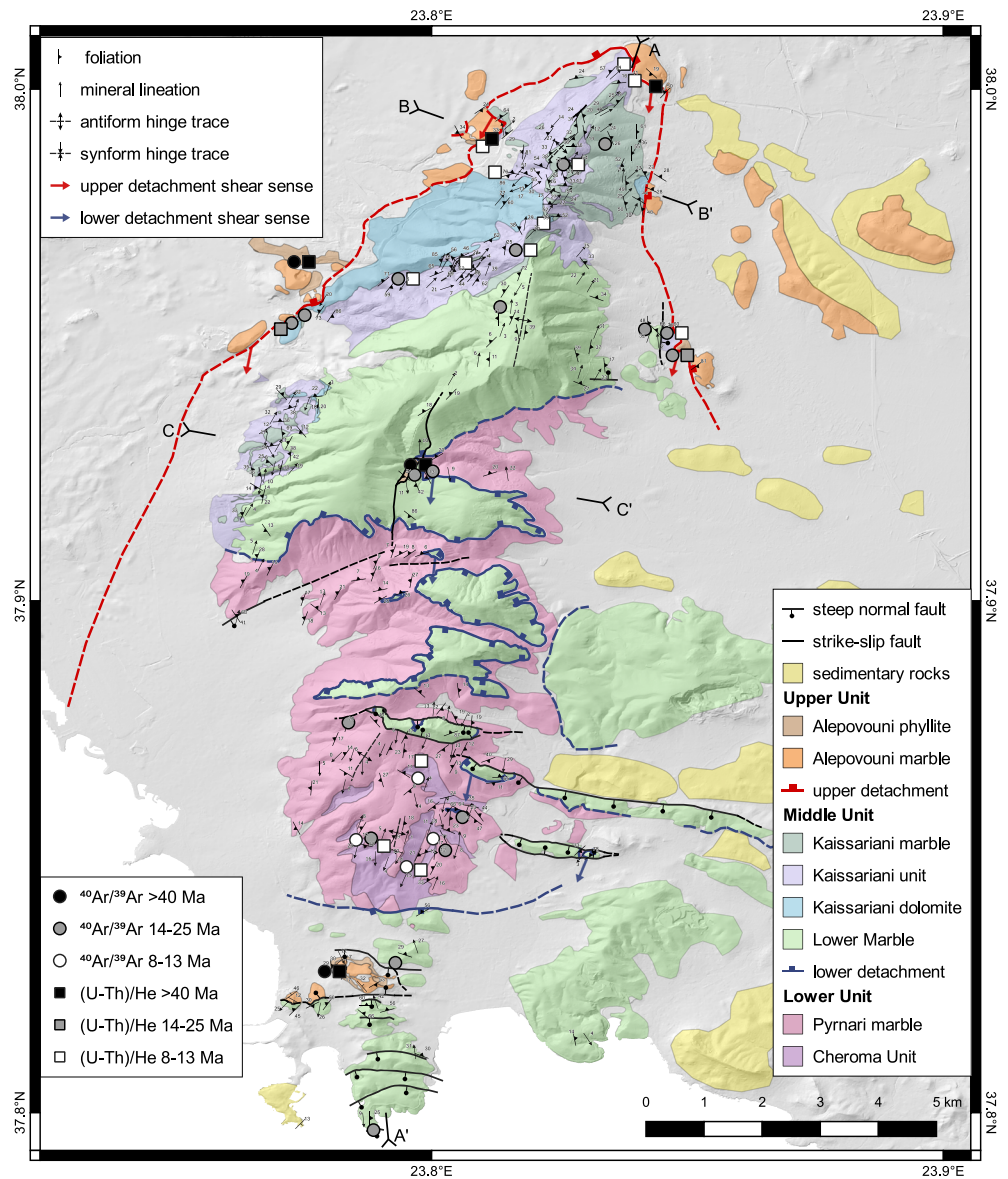
Figure 2. Geologic map of Mt. Hymittos, Greece, based on new bedrock mapping and maps of Lepsius (1893), Lekkas and Lozios (2000), and Latsoudas (2003). Map shows structural measurements (foliation and lineation) and location of geochronology samples (with ages). See Figure S1 for more information. Cross-section markers correspond to the profiles in Figure 3. The unmetamorphosed rocks of the Mesogea and Athens basins as well as those underlying them have been grouped into the sedimentary rocks unit. The map is projected in the Universal Transverse Mercator (UTM) coordinate system, zone 35°N, using the World Geodetic System (WGS) 1984 datum.

3. Methodology

In order to investigate the tectonic history of Hymittos, we combine bedrock mapping, structural and petrographic analysis, electron microprobe analyzer (EMPA) analysis, and multiple single-grain total-fusion white mica ^{40}Ar/^{39}Ar and zircon (U-Th)/He geochronology on samples from the Upper, Middle, and Lower units of Hymittos. We focused on mica-bearing metasedimentary rocks, including calcitic and dolomitic marbles, mica schists, and calc-mica schists. White mica ^{40}Ar/^{39}Ar dating was conducted at the University of Manitoba using a multi-collector Thermo Fisher Scientific ARGUSVI mass spectrometer. Zircon (U-Th)/He dating was carried out at the University of Colorado-Boulder on a Balzers PrismaPlus QME 220 quadrupole mass spectrometer. EMPA mineral chemical analyses and
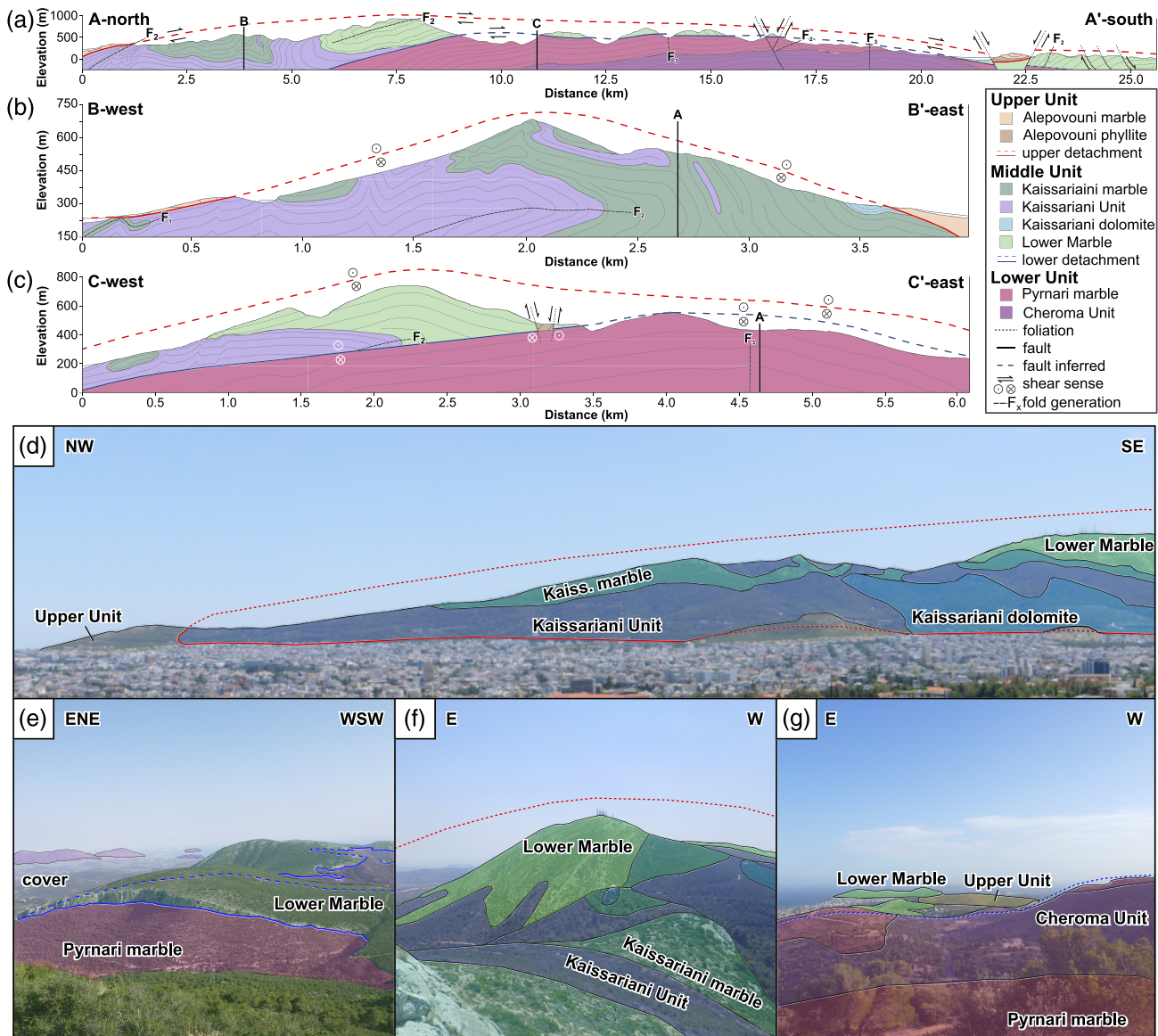
Figure 3. (a) N-S geological cross section of Hymittos massif drawn at 1:1 scale. Structural styles differ across the massif. In north and central Hymittos, the detachments shape the topography producing a north-dipping dip slope and a series of klippen. Shear sense along both detachments is top-S. In southern Hymittos, a graben and asymmetric, listric, high-angle normal faults have developed. These faults cross-cut and offset the detachments as part of a graben. (b) W-E geological cross section of the bedrock of northern Hymittos massif drawn at 1:1 scale. Middle Unit schist and marble are folded together as part of a km-scale recumbent fold. (c) W-E geological cross section of the bedrock of central Hymittos massif drawn at 1:1 scale. Syn-orogenic structures preserved in the Middle Unit are truncated by the post-orogenic lower detachment. (d) Field photo of the upper detachment in northern Hymittos taken from 38.023665°N, 23.76793°E. The Upper Unit hanging wall (orange) is composed of the phyllites and marbles of the Alepovouni Unit. The Middle Unit footwall is the intercalated schists and marbles of the Kaissariani Unit (blue), the Kaissariani dolomite (light blue), the Kaissariani calcitic marble (dark green), and the calcitic Lower Marble (light green). Lithology colors correspond to colors on the geology map (Figure 2). (e) Exposures of the lower detachment in central Hymittos; photo taken from 37.94068°N, 23.8038°E. The footwall is a Lower Unit (violet) dolomitic marble mylonite (Pyrnari Marble), the hanging wall is a Middle Unit (green) calcitic (Lower Marble) mylonite. (f) Folded and intercalated Middle Unit rocks in northern Hymittos including Kaissariani Unit schist (dark blue), marble (forest green), and the Lower Marble (light green). Photo taken from 37.97992°N; 23.82409°E. (g) Exposures of the Upper, Middle, and Lower units in southern Hymittos; photo taken from 37.85850°N, 23.80152°E. Middle Unit is composed of the Lower Marble (green), Lower Unit is valley-forming Cheroma Unit (purple) and ridge-capping Pyrnari Marble (violet).

associated EDS mapping were carried out using a JEOL JXA-8230 SuperProbe and JEOL 6610LV SEM at the University of Ottawa. Detailed methodologies, data tables, and additional figures are available in the supporting information.
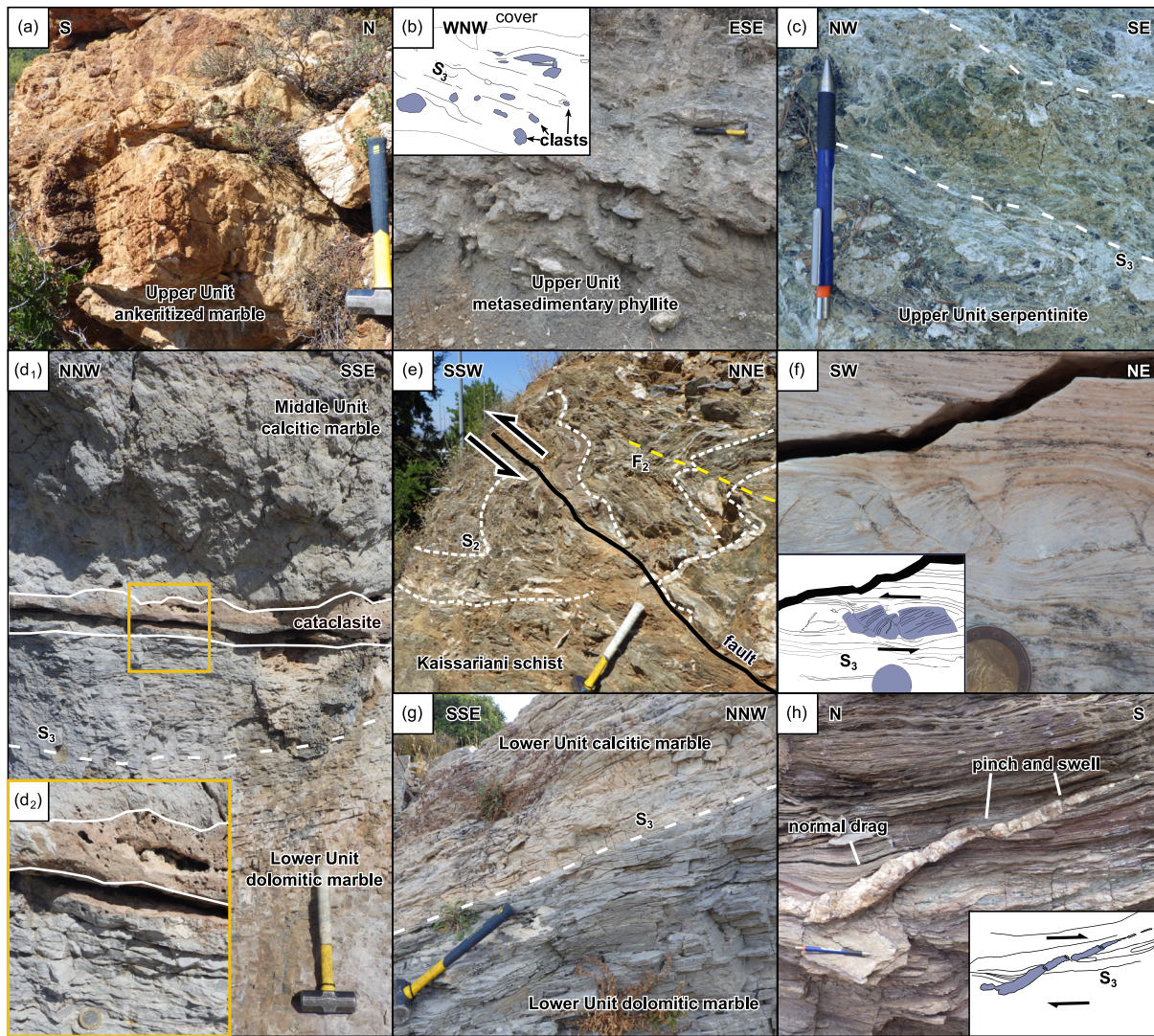
Figure 4. (a) Roughly bedded, ankeritized Upper Unit Alepovouni marble, 8 m above the upper detachment (37.95868°N; 23.77806°E). (b) Upper Unit (Alepovouni Unit) low-grade, foliated, cataclased metasedimentary phyllites with sheared, flattened clasts. Upper Unit phyllites are commonly heavily weathered (37.828016°N; 23.781051°E). (c) Cataclased serpentinite and metasediment melange exposed along the Upper Detachment (38.000546°N; 23.843805°E). (d_1) Outcrop exposing brittle fault rocks of the lower detachment. The hanging wall is a cataclased calcitic marble mylonite; the footwall is a brittlely deformed, dolomitic marble ultramylonite. (d_2) The fault core is composed of ultracataclasite cut by a sharp fault plane (37.90942°N; 23.79802°E). (e) Recumbent (F_2) folds in Middle Unit calc-schist in NW Hymittos. Two generations of veins are visible, an initial generation predates foliation (S_2) development and is folded with the foliation; the second vein generation cross-cuts the folds. Outcrop is cut by an apparent thrust fault that produced fault drag folds (37.98398°N; 23.81199°E). (f) Apparent top-SW shear sense inferred from domino boudinage of a dolomitic interlayer within a calcitic Middle Unit marble mylonite (Lower Marble; 37.95949°N; 23.83243°E). (g) Calcitic and dolomitic Lower Unit mylonitic marbles. Contact between the two is gradational over a few centimeters (37.85974°N; 23.80189°E). (h) Top-S shear sense inferred from A-type flanking fold developed along a boudinaged quartz vein in Lower Unit (Cheroma Unit) calc-schist. Vein offsets also indicate top-S shear (37.85258°N; 23.79088°E).

4. Hymittos Mountain

New bedrock geology mapping of Hymittos identified a local tectonostratigraphy dominated by three tecto-nostratigraphic units (herein Upper, Middle, and Lower units, local names after Lepsius, 1893) separated by ductile-then-brittle low-angle normal faults (Figures 2 and 3). Away from the massif these units are overlain and obscured by late Miocene to Pleistocene sedimentary rocks of the Athens and Mesogea basins (e.g., Lepsius, 1893; Marinos & Petraschek, 1956; Marinos & Symeonidis, 1974; Papanikolaou, Bassi, et al., 2004, and references therein). The following sections synthesize field observations and structural and
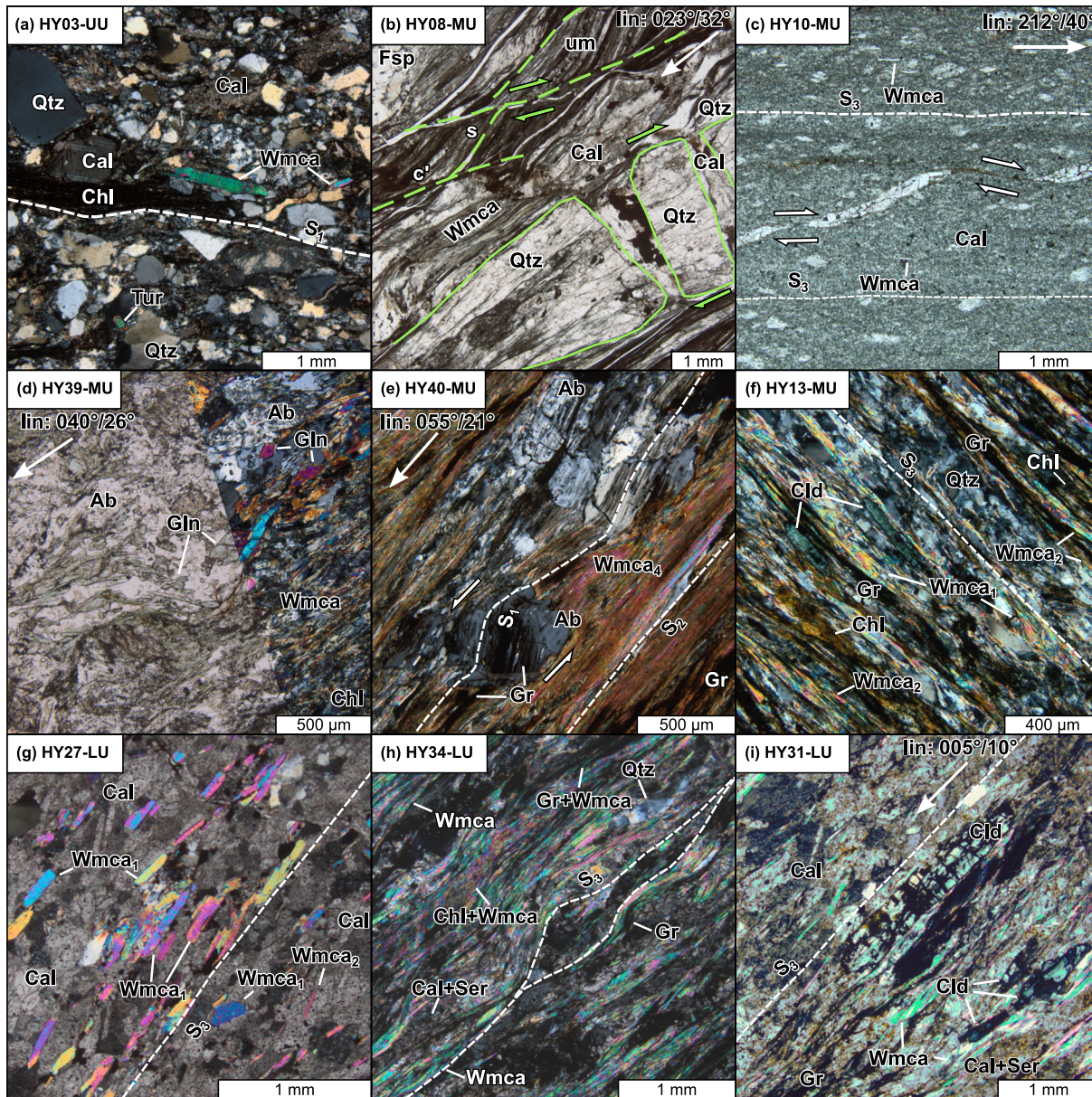
Figure 5. (a: HY03: 37.82802°N; 23.78105°E) XPL photomicrograph of Upper Unit metasedimentary phyllite white mica that form a single population of 100–1,000 μm long, brittlely deformed, kinked, subhedral to anhedral crystals. (b: HY08: 37.955294°N; 23.774308°E) PPL photomicrograph of Middle Unit white mica, calcite, feldspar, quartz, ultramylonitic schist. Top-S sense of shear inferred from S-C′ fabrics in dark ultramylonite bands and rotation of domino boudinaged quartz microlithons. (c: HY10: 37.954109°N; 23.842426°E) PPL photomicrograph of Middle Unit calcitic marble mylonite. Top-S shear sense inferred from shear band boudinaged calcite vein. (d: HY39: 37.963677°N; 23.807964°E) Composite PPL and XPL photomicrograph of Middle Unit glaucophane-bearing metabasic schist. M_1 glaucophane is preserved as part of a relict S_1 foliation in albite porphyroblasts. (e: HY40: 37.963923°N; 23.803121°E) XPL photomicrograph of Middle Unit quartz graphite chlorite albite white mica schist. Albite porphyroblasts exhibit apparent top-N shear during top-N rotation. Graphite in albite porphyroblasts preserves an earlier generation of the foliation S_1, rotated during a second generation of deformation synchronous with metamorphism evinced by curved graphite foliation in the clearer rims of the albite porphyroblasts. The S_2 foliation is comprised of white mica, graphite and chlorite. (f: HY13: 37.96293°N; 23.79347°E) XPL photomicrograph of Middle Unit mylonitic metasedimentary schist, where white mica comprise two populations: $Wmca_1$ 100–250 μm long subhedral crystals oriented oblique to foliation within quartz- and feldspar-rich microlithons. $Wmca_2$ elongate 100–500 μm long, subhedral-to-anhedral, kinked crystals within shear bands; commonly interlayered with graphite, and/or chlorite. (g: HY27: 37.85127°N; 23.80268°E) XPL photomicrograph of Lower Unit calcitic marble mylonite, where white mica comprise two populations: $Wmca_1$ 200–800 μm long euhedral crystals oriented parallel to the S_3 foliation. $Wmca_2$ 50–100 μm long euhedral crystals oriented parallel to the foliation in calcitic and dolomitic marble mylonites. (h: HY34: 37.85355°N; 23.80040°E) XPL photomicrograph of Lower Unit mylonitic pelitic schist, where white mica are elongate 100–500 μm long, extensively sheared and deformed subhedral-to-anhedral, crystals forming shear bands in mylonitic mica schist and calc-mica schist; commonly interlayered with graphite, and/or chlorite. (i: HY31: 37.86536°N; 23.797344°E) XPL photomicrograph of chloritoid-white mica calc-schist. Qtz: quartz, Cal: calcite, Wmca: white mica, Ser: Sericite, Chl: Chlorite, Fsp: Feldspar, Ab: Albite; Gr: Graphite, Cld: Chloritoid, Gn: Glaucophane, S_1: 1st foliation, s_2: 2nd foliation (mineral abbreviations from Siivola & Schmid, 2007).

petrographic analyses conducted on rock samples from the Upper, Middle, and Lower units of Hymittos; detailed petrographic results are available in Table S1.

4.1. Upper Unit

The upper tectonostratigraphic package of Hymittos (herein Upper Unit; locally Alepovouni Unit) consists of low-grade metasiliciclastic phyllites, serpentinites, marbles, and ophiolitic rocks (Figures 4a, 4b, and 4c). The Upper Unit is primarily exposed at the margins of the northern massif; there are smaller exposures preserved in a dextral pull-apart basin in the central massif and a graben in the southern foothills (Figure 2). Upper Unit calc-phyllites and phyllites typically have a calcite-sericite-chlorite-white mica-quartz-plagioclase feldspar $\pm$ tourmaline $\pm$ epidote mineralogy and are bedded on a 1–10 cm scale. Most phases are anhedral to subhedral, frequently angular, and evince a foliation and shape-preferred orientation development (Figures 5a and S4a). Upper Unit marbles display several generations of calcite veining and elongate calcite ribbons (Figure S4b). Upper Unit serpentinites and serpentinized phyllites exhibit a calcite-talc-epidote-quartz-chlorite-serpentinite mineralogy (Figure S4c). Bedding thicknesses of Upper Unit marble range from 50 cm to >1 m, and primary bedding is weakly expressed. Folded metachert layers at some outcrops indicate deformation of these marbles must have occurred at some point. Foliations are typically low-angle and mineral and stretching lineations show a large dispersion; at lower structural levels approaching the upper detachment, the lineations are oriented N-S (Figures 6e and 6j). The mineral assemblages of the Upper Unit suggest low-grade metamorphic conditions of prehnite-pumpellyite to lowest greenschist facies. Micro and macrostructures suggest a single episode of foliation development related to isoclinal folding (F_1; Figures 4b and 4c), followed by a generation of open folding (F_2) with shallowly north-plunging fold hinges and subvertical axial planes.

4.2. Middle Unit

The middle tectonostratigraphic package of Hymittos bedrock (herein Middle Unit comprising the Kaissariani Unit and Lower Marble; locally Kaissariani Schist, Upper Marble, and Lower Marble) consists of the greenschist facies metasedimentary and metavolcanic schists (Figures 4e, 5b, and 5d) and calcitic and dolomitic marbles (Figures 4f and 5c). The schistose lithotypes are a calcite-chlorite-graphite-quartz-white mica $\pm$ feldspar $\pm$ chloritoid metasedimentary schist (Figure 5f) and epidote-chlorite-graphite-quartz-albite-white mica $\pm$ feldspar metavolcanic schist (Figure 5d). Quartz microlithons in Middle Unit metabasic schists uncommonly preserve glaucophane crystals and metapelitic calc-schists exhibit chloritoid, which is often replaced by chlorite and white mica (Figure 5e). This relationship suggests initial high-pressure metamorphism followed by greenschist facies retrogression. Schistose rocks form dm- to m-thick layers that are intercalated and folded together with blue-grey calcitic marble mylonites. At higher structural levels, and to the east, the proportion of calcitic marble increases (Figures 2, 3a, and 3d), and the mylonites become paler in color. Within these interfolded mylonites are cm- to km-scale pervasively fractured dolomite blocks containing Triassic corals (Négris & Meunier, 1915) and rare quartzite and serpentinite. At the highest structural levels, along the upper detachment are exposures of a cataclased epidote-serpentinite mélange. Ultramylonitic bands are common in samples close to the upper detachment (Figure 5b). Middle Unit marbles exhibit a dominantly calcitic mineralogy with minor white mica. The calcitic marbles are mylonitic with grain sizes ranging from 50 to 15 μm and display a 30–60° dipping S_{1-2} foliation (Figure 6a). Middle Unit dolomitic blocks are commonly weakly to non-foliated and brittlely deformed with a tectonically reworked sedimentary contacts adjacent to calcitic marble. The Middle Unit is present as a series of steeply foliated (S_2) calcitic marble klippen above the lower detachment in central Hymittos and within the foothills east and south of the massif (Figures 2 and 3a).

The greenschist facies rocks of the Middle (and Lower) units exhibit a regional-scale foliation delineated by alternating marble and schist layers. In northern and north-central Hymittos, highly attenuated, tight to isoclinal folds are preserved within laterally extensive mylonitic layers suggesting an early F_1 folding event that reoriented an initial S_1 foliation (Figure 6a). These F_1 folds are overprinted and sheared into an S_2 foliation associated with rarely preserved WNW-ESE lineations (L_2) producing a regional-scale S_{1-2} transposition foliation (Figures 6a and 6f). The schist and marble layers that define this variably dipping S_{1-2} foliation are themselves folded (F_2) into km-scale recumbent folds with NNE-SSW hinges (Figures 3b and 6b). S_{1-2} foliation orientations vary across the massif as they have been reoriented by both F_2 and F_3 fold
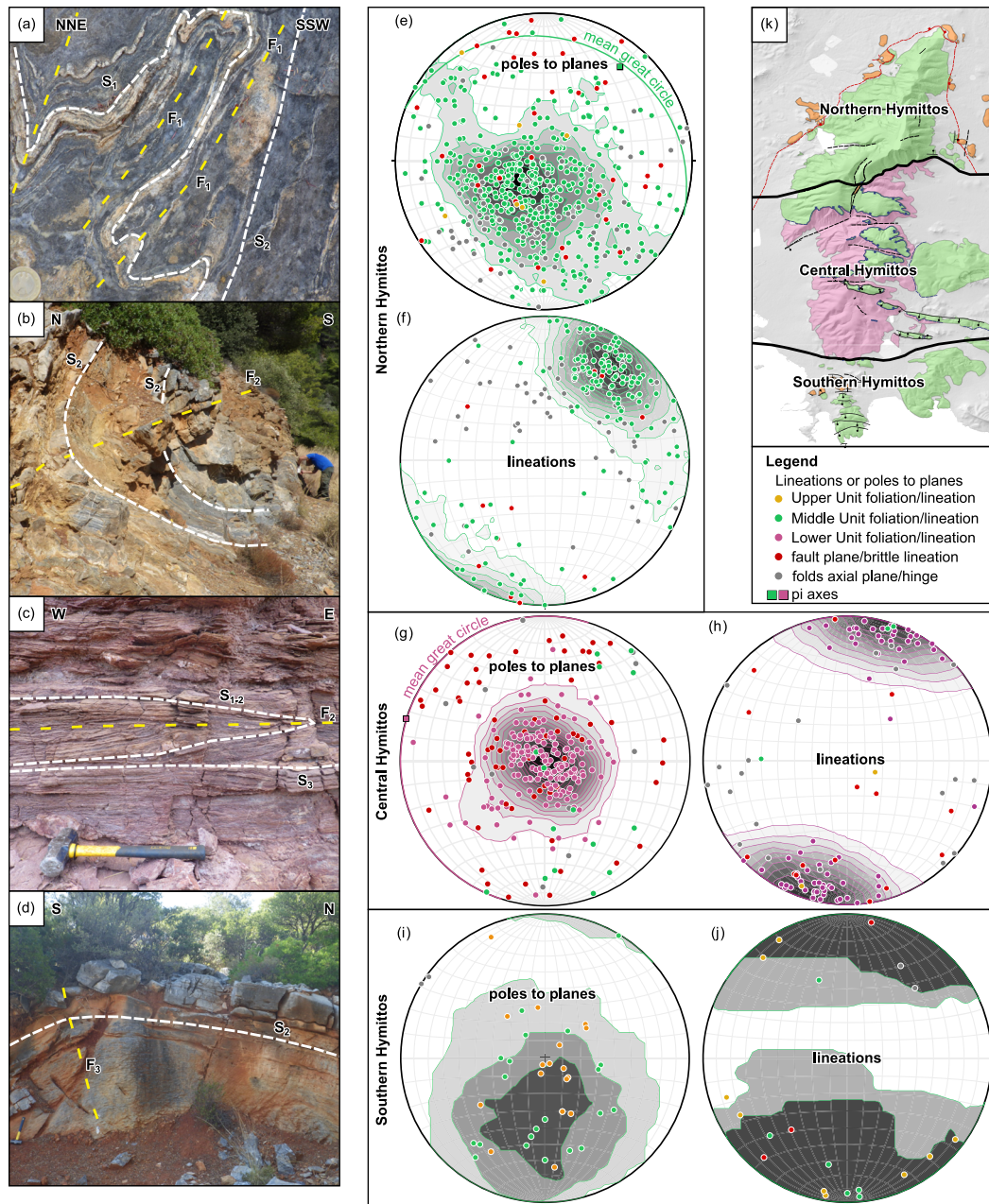
Figure 6. Outcrop images of structural elements (a-d) and equal-area lower hemisphere stereograms of planar and linear structural elements (e-j). (a) S_1 foliation refolded by F_1 folds and transposed into the S_2 foliation in Middle Unit calcitic marble (37.98275°N; 23.82005°E). (b) S_2 foliated Middle Unit marble and calc-schist folded by recumbent F_2 folds in northern Hymittos (37.96591°N; 23.80582°E). (c) Isoclinally folded S_{1-2} foliation as a product of S_3 transposition foliation in Lower Unit quartz-mica schist (37.85335°N; 23.78549°E). (d) Foliated (S_2) and open F_3 folded calcitic Middle Unit marble in northern Hymittos (37.99040°N; 23.834621°E). (e) Stereogram of poles to planes of Upper and Middle unit planar elements in northern Hymittos. Ductile foliations have been contoured illustrating a broadly flat-lying foliation pattern related to reorientation of steeper dipping S_1 and S_2 foliations during D_3 deformation. Axial planes of folds are generally steeply to shallowly north dipping. Faults are moderate to steeply dipping with many orientations. (f) Stereogram of Upper and Middle Lower unit linear elements in northern Hymittos. Note the dominant relatively shallow NE-SW post-orogenic lineation (L_3) overprinting most of the E-W and ENE-WSW synorogenic lineations (g) Stereogram of poles-to-planes of Upper, Middle and Lower unit planar elements in central Hymittos. S_3 deformation was more pervasive in these units and fully transposed most earlier structures, resulting in relatively little dispersion in measurements. (h) Stereogram of Upper, Middle and Lower unit linear elements in central Hymittos. Lineations contoured populations are more uniform and rotated slightly counterclockwise compared to Middle Unit lineations in northern Hymittos. F_3 fold hinges are both E-W and N-S oriented. (i) Stereogram of poles-to-planes of Upper and Middle unit planar elements in southern Hymittos. While the pole to foliation contouring is imprecise due to relatively low measurements, the distribution has a similar orientation to measurements from the Middle Unit in northern Hymittos. (j) Stereogram of Upper and Middle unit linear elements in southern Hymittos. See inset diagram for delineation of northern, central and southern Hymittos. Poles to planes of folds (grey): axial planes, fold lineations (grey): hinges. Mean great circles were calculated using a cylindrical best fit. Stereograms plotted using Stereonet (Cardozo & Allmendinger, 2013).

generations. Parasitic s-, z-, and m-folds distributed along the margin of the Lower Marble-Kaissariani Unit contact indicate that the Kaissariani Unit is folded around the Lower Marble, underlying it in the southwest and occurring adjacent to and above it in the northwest. The weakly developed girdle illustrated in the contoured poles to Middle Unit foliation planes is the product of folding of S_2 foliations around the ~NE-SW fold hinge (Figure 6e). Middle Unit axial planes show a similar E-W dispersion (Figure 6e). Dolomitic (or high-Mg calcite) layers within the calcitic Middle Unit marble mylonites of the massif are boudinaged in E-W and N-S directions and have been rotated with a top-SSW sense of shear (Figure 4f).

At higher structural levels, close to the upper detachment ultramylonitic marbles are more common with 10–3 μm sized calcite grains defining a subhorizontal S_3 foliation; sheared calcite and quartz veins preserve a top-SSW sense of shear (Figure 5c). Schistose lithotypes at similar structural levels contain ultramylonitic bands with top-SSW S-C fabrics (Figure 5b).

4.3. Lower Unit

The lower tectonostratigraphic package of Hymittos bedrock (herein Lower Unit; locally Vari Schist, Pyrnari Marble) consists of greenschist facies pelitic schist, calc-schist, calcitic and dolomitic marbles, and rare quartzite (Figures 4g, 4h, 5g, 5h, and 5i). In the central massif, exposures of the Lower Unit comprise >200 m thick, medium-to-dark grey, variably carbonaceous dolomitic marbles (Pyrnari Marble); at higher structural levels, these marbles transition from largely undeformed to a strongly S_3-parallel foliated mylonite (50–20 μm grain size) and ultramylonite (3–5 μm grain size). In southcentral Hymittos, the mylonitic marble is 20–30 m thick and variably calcitic to dolomitic in composition (Figure 4g).

Deeper structural levels expose intercalated metasiliciclastics and marbles of the Cheroma Unit. Historically termed the Vari Schist (Lepsius, 1893), we propose renaming this unit to avoid confusion with the Vari Unit on Syros (e.g., Aravadinou & Xypolias, 2017; Soukis & Stockli, 2013), as well as the presence of both marbles and schistose lithotypes within the Vari Schist. Cheroma is the local term for the valley in southern Hymittos that best exposes the proposed type section. Cheroma schists and calc-schists have a calcite-chlorite-graphite-quartz-white mica $\pm$ chloritoid $\pm$ tourmaline mineralogy and are intercalated with fine-grained calcitic and dolomitic marble mylonites and rare quartzite (Figures 5g, 5h, and 5i). Cheroma quartzites are fine- to medium-grained with a quartz-white mica-tourmaline-apatite mineralogy and display grain boundary subgrain rotation, incipient grain-boundary bulging and a well-developed top-S grain-shape preferred orientation (S_3). White mica, chlorite, and graphite occur as top-S shear bands; quartz defines distinct microlithons which may contain chloritoid aligned in a N-S orientation. Cheroma marbles are calcitic and dolomitic mylonites with grain sizes ranging from 50–20 μm and trace foliation-parallel coarse-grained white mica. Cheroma Unit rocks exhibit an F_2 refolded S_{1-2} foliation most evident in schists and calc-schists.

4.4. Ductile-Then-Brittle Faulting

The Upper, Middle, and Lower units are separated by a pair of top-SSW, ductile then brittle, low-angle normal detachment faults (Figures 2 and 3). The ductile deformation associated with the detachments commonly extends >100 m into the footwall producing N-S oriented, L-S tectonites, mylonites, and ultramylonites in both marbles and schists. The structures have clear top-SSW kinematics determined from flanking folds, sigmoids, delta clasts, stair-stepping of strain shadows on porphyroclasts, domino boudinage, and SCC′ fabrics within this zone of ductile deformation (Figures 4f, 4h, 5d, 5h, and 5k). Both detachment faults exhibit cataclastic fault cores that grade into the lithologies of their respective hanging walls (Figures 4d and S4j); imbrication of clasts within the cataclasite bands gives a top-S sense of shear. The low-grade marble of the Upper Unit is heavily ankeritized close to the upper detachment, suggesting the detachments was a conduit for Fe-rich fluids (Figure 4a). Serpentinite and metavolcanic lenses are present within the fault zone of the upper detachment (Figure 4c).

Close to the upper detachment in the Middle Unit, and pervasively within the Lower Unit in central and southern Hymittos, the F_2 folded S_{1-2} foliation is overprinted by a shallowly dipping mylonitic S_3 foliation with an associated NNE-SSW lineation (L_3; Figures 6f, 6h, and 6j) that increases in intensity with proximity to the detachments. The L_3 lineation is much more strongly expressed and uniform than the S_3 foliation, NNE-SSW-oriented lineations are uniformly present in the Lower Unit in almost all instances; these L_3 lineations are somewhat more dispersed in the Middle Unit than in the Lower Unit (Figures 6f, 6h, and 6j). The S_3 foliation transposes previous folds and rotates fold hinges into a NNE-SSW orientation producing

a second generation of isoclinal folds (Figure 6c). The S_3 foliations and all earlier structures are folded by F_3 domal open folds with vertical axial planes and both N-S and E-W hinges (Figures 6d, 6e, and 6g).

Flanking structures in both the Middle and Lower units are dominantly top-SSW, though uncommon top-NNE structures are observed; consistent with a top-SSW regime, as antithetically rotating flanking structures may form under general shear (Wiesmayr & Grasemann, 2005). Several generations of veins within Middle and Lower unit rocks preserve evidence of progressive shearing; earlier vein generations are fully transposed into the S_2 and S_3 foliations and are folded by F_2 and F_3 folds. Younger veins crosscut the S_2 foliation and F_2 folds and are only sheared and folded where S_3 and F_3 structures are evident.

Several populations of steeply-dipping normal faults are observed (Figure 2). In north and central Hymittos, steeply-dipping E-W normal and N-S strike-slip faults have been identified in several instances; no definitive cross-cutting relationships have been observed. In southernmost Hymittos, well developed normal faults have rotated foliated Middle Unit marble into a steep orientation (Figure 3a). These south-dipping faults are evident on satellite imagery and based on their orientation may root into the lower detachment.

4.5. White Mica Compositions

White mica ^{40}Ar/^{39}Ar geochronology requires characterizing the potential white mica populations in the sample. Through optical petrography, EDS mapping, and EMPA analysis, multiple populations of white mica have been identified based on grain size, host lithotype, degree of crystal plastic deformation, and geochemistry.

White mica from Upper Unit phyllites exhibit a single population of 100–1,000 µm long, brittlely deformed, kinked, subhedral, to anhedral crystals with minimal undulatory extinction (Figures 5a and S4d). Where the phyllites possess a foliation, these crystals may display a weak preferential alignment. In some instances, chlorite-white mica intergrowths can be observed (Figure S4d). EDS chemical mapping and EMPA analysis were not conducted on white mica from Upper Unit samples as these samples are low-grade metasedimentary rocks from the hanging wall and are not expected to have experienced the Tertiary metamorphic history of the CBU.

Optical petrography identified five white mica populations within samples from the Middle Unit rocks. Two populations are recognized in Middle Unit marbles. (1) 50–250 µm long euhedral crystals oriented parallel to the foliation in calcitic marble mylonites (Figures 5c, S4e, and S6b). (2) In certain mica rich marble samples, white mica crystals are 200–500 µm long, anhedral to euhedral and exhibit weak interlinked mica layers, and some kinking and undulose extinction, indicating some degree of deformation, but no strong shear (Figure S4f). Populations 1 and 2 are dominantly moderate-Si phengite, with minor muscovite intergrowths and rims though exceptions exist (Figures S2 and S6; Table S2). The calc-mica schist and mica schist of the Middle Unit host an additional three populations. (3) Subhedral 100–250 µm long crystals oriented oblique to the S_3 foliation within quartz- and feldspar-rich microlithons (Figures 5f and S6e); (4) elongate 100–500 µm long, subhedral-to-anhedral, kinked muscovite crystals within shear bands; commonly interlayered with graphite, more rarely chlorite (Figure 5f); and (5) anhedral, 50–100 µm long, phengitic or less commonly muscovitic crystals forming the cores of mica fish (Figures 5f and S2).

Optical petrography identified four white mica populations within samples from Lower Unit rocks. (1) Euhedral 200–1,000 µm long crystals oriented parallel to the foliation in calcitic marble mylonites (e.g., Hy27, Figures S2, 5g, and S6c), these crystals are dominantly moderate-Si phengite but exhibit muscovite-adjacent Si values (e.g., Hy 28; Figure S2). (2) Euhedral 50–100 µm long phengitic crystals oriented parallel to the foliation in calcitic and dolomitic marble ultramylonites these crystals exhibit sparse muscovitic rims (e.g., Hy26, Figures S2 and 5g). (3) Elongate 100–500 µm long, extensively sheared and deformed subhedral-to-anhedral crystals forming shear bands in mylonitic mica schist and calc-mica schist; commonly interlayered with graphite, and more rarely chlorite (Figures 5h, S2, and S6d). (4) Subhedral-to-anhedral, 100–700 µm long, moderately deformed crystals in less mica rich calc-mica schists (Figures 5i and S6a).

White mica in Middle and Lower unit marbles typically possess a phengitic composition (Figure 7b) trending from a median composition between Al-celadonite along the Tschermak substitution to a muscovite-rich end member (Figures 7a and 7c; Table S2); white mica in schistose rocks exhibit a slightly more
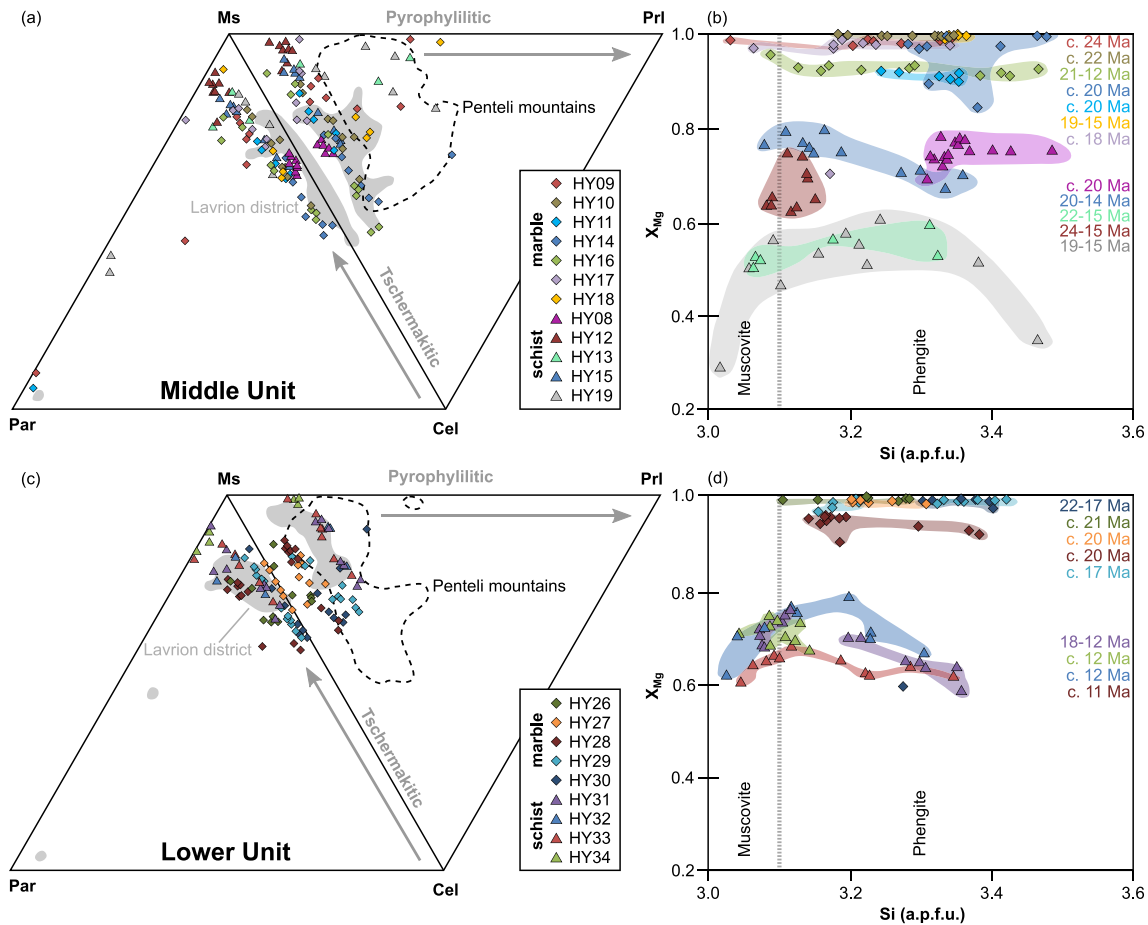
Figure 7. Mica chemical compositions. (a) Muscovite (Ms)-celadonite (Cel)-paragonite (Par) and muscovite-celadonite-pyrophyllite (Prl) chemistry ternary diagrams for the Middle Unit marble (diamonds) and schist (triangles) of Hymittos. Dashed field: white mica analyses from the upper tectonic unit of Penteli (Baziotis et al., 2019); grey field: analyses from the middle tectonic unit of the Lavrion district (Coleman et al., 2019). (b) Silicon (Si) in atoms per formula unit (a.p.f.u.) versus relative magnesium concentration (X_{Mg}) binary diagram for Middle Unit white mica. White mica analyses define two populations divided by lithotype. (c) Ms-Cel-Par and Ms-Cel-Prl chemistry ternary diagrams for marble and schist of the Lower Unit of Hymittos. White mica analyses are displayed from the lower tectonic unit of Penteli (dashed field; Baziotis, Mposkos, et al., 2019) and the lower tectonic unit of the Lavrion district (grey field; Coleman et al., 2019). (d) Silicon (a.p.f.u) versus X_{Mg} binary diagram for Lower Unit white mica. Mica form two populations divided by lithotype. Endmember calculations followed the methodology of Parra et al. (2002) and Vidal and Parra (2000). The mica nomenclature and compositional fields are from Rieder et al. (1998). The weighted average of $^{40}Ar/^{39}Ar$ total fusion analyses are listed for each sample in (d) and (e).

muscovitic composition. Both in marbles and schists, white mica shows a greater compositional heterogeneity in the Middle Unit (marble: 40–86% muscovite; schist: 49–89% muscovite, except one outlier; Figure 7a; Table S2) compared to the Lower Unit yielding more muscovitic analysis (marble: 56–82% muscovite, schist: 59–91% muscovite Figure 7c; Table S2). This is comparable to mica compositions in the middle and lower tectonic units of Lavrion (Coleman et al., 2019), though white mica from Hymittos show an overall greater range of compositions. The degree of pyrophyllitic substitution is higher in Middle Unit samples compared to Lower Unit samples, analogously to observation in the upper and lower unit of the nearby Penteli Mountains (Baziotis, Mposkos, et al., 2019). Individual samples show a substantial degree of compositional heterogeneity. EDS maps combined with WDS point data reveal compositional zoning with phengitic, high-Si cores and muscovitic, low-Si rims fairly pronounced in Middle Unit rocks (e.g., Hy17; Figure S2) and to some extent also in Lower Unit rocks. In populations 2, 3, and 4 of the Middle Unit and 2, 3, 4, and 5 of the Lower Unit occasional intergrowths of chlorite and rare paragonite were observed. Compositional variability is particularly common in shear bands, where white mica is intergrown with chlorite and graphite (Figures 5h, S2, S4, and S6).
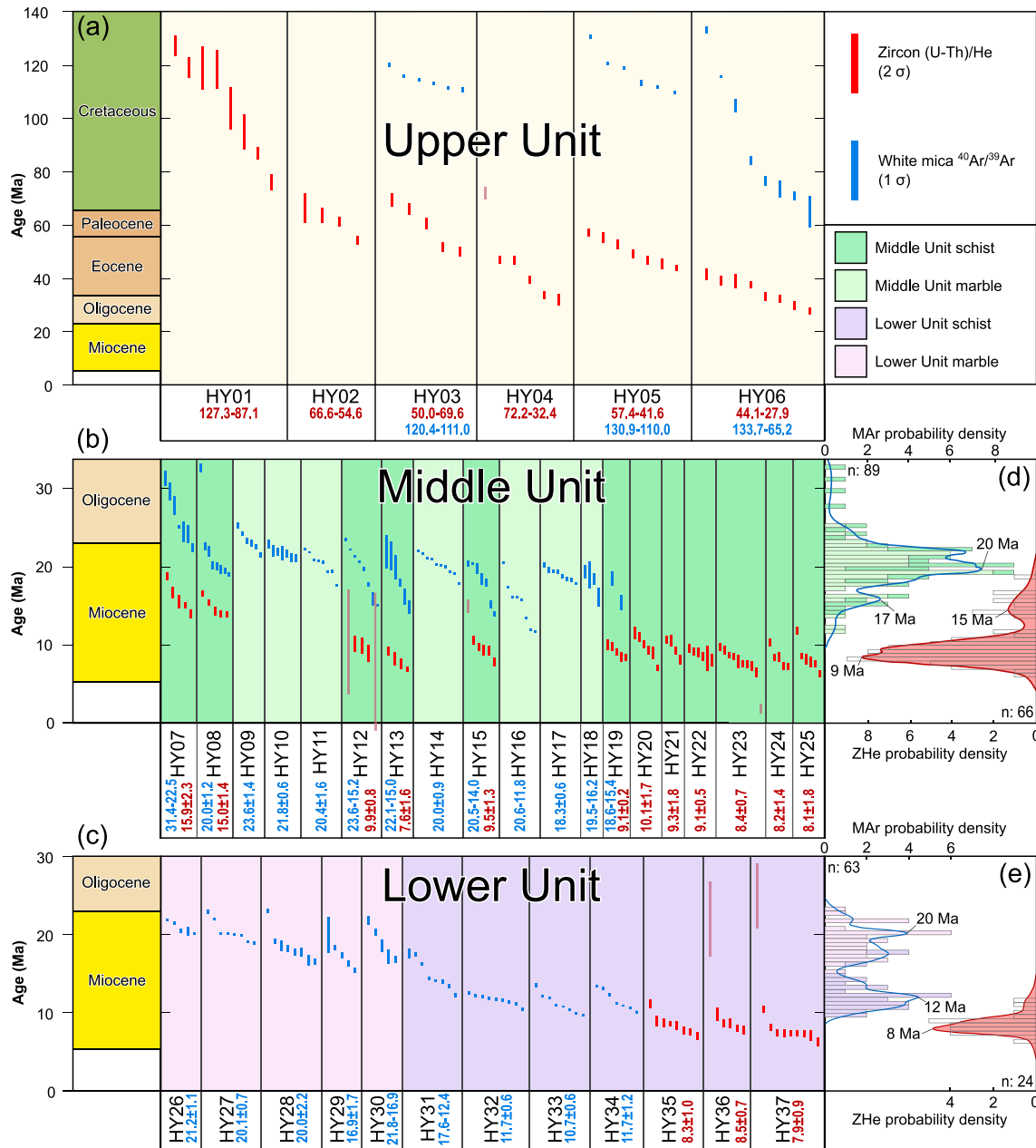
Figure 8. Summary of new geochronology from Hymittos. (a, b, c) Weighted distribution diagrams and (d, e) kernel density estimates for white mica ^{40}Ar/^{39}Ar total fusion (MAr; blue) and zircon (U-Th)/He (ZHe; red) ages. All ZHe ages are from (meta)siliciclastic rocks; MAr ages from marbles and schists. Grey bars are rejected analyses. Weighted average ages (when permissible) for both techniques are calculated for each sample. Two Devonian ^{40}Ar/^{39}Ar ages (337.5 ± 0.7 Ma, HY03 and 369.2 ± 1.7 Ma, HY05) and a single early Jurassic ^{40}Ar/^{39}Ar age (199.7 ± 0.8 Ma, HY05) are not displayed. See data repository for ^{40}Ar/^{39}Ar and (U-Th)/He analytical data tables (Tables S3 and S4) and sample locations (Figure S1).

The division between marble and schistose white mica populations is best evident on the Si (a.p.f.u.) versus relative Mg concentration $\left(X_{Mg} = \dfrac{Mg}{Fe + Mg}\right)$ binary diagrams (Figures 7b and 7d). White mica from Middle and Lower unit marbles exhibit X_{Mg} values larger than 0.8 (except one outlier) whereas X_{Mg} in Middle and Lower unit schists ranges from 0.4 to 0.8 (Figures 7b and 7d), with individual samples forming distinct populations with respect to X_{Mg}. As no overlap occurs between the schist and marble samples, and there is no observable trend between Si and X_{Mg}, the difference in X_{Mg} between schists and marbles and also individual samples is likely controlled by bulk-rock composition rather than changing metamorphic conditions.

In contrast, Si (a.p.f.u.) values of schist and marbles largely overlap between 3.0 and 3.5. It is noted however that in the Lower Unit white mica from schistose samples exhibit lower Si (a.p.f.u.) than white mica in marble samples (Figure 7d). Maximum Si (a.p.f.u) values reach up to 3.5 in the Middle Unit and 3.4 in the Lower Unit. Irrespective of lithology in the tectonic unit, considerable intrasample dispersion is observed in some cases. More or less continuous variation along the Tscherkmak substitution and evidence of multiple white mica populations suggests that the intra-sample dispersion in mineral composition is likely indicative of subtly changing P-T conditions during (neo/re)crystallization events (Parra et al., 2002).

4.6. White Mica ^{40}Ar/^{39}Ar Geochronology

Multiple single-grain total fusion white mica ^{40}Ar/^{39}Ar analyses were conducted on up to eight grains for 25 mica-bearing rock samples from Hymittos. Three Upper Unit, 13 Middle Unit, and nine Lower Unit samples were analyzed (Figures 2 and S1 for sample locations). Weighted average ages are reported for samples where dispersion is low and age ranges for samples where dispersion is high (1σ; Figure 8; Table S3). Total fusion is a useful technique as it constrains age heterogeneity both within a sample and across multiple samples (e.g., Coleman et al., 2019; Schneider et al., 2018; Uunk et al., 2018).

Analysis of 23 single grains from three Upper Unit samples produced ages that range from the Late Devonian (369.3 ± 1.8 Ma) to the earliest Paleocene (65.2 ± 5.6 Ma). A Cretaceous to early Paleocene age population (*n*: 20; Figure 8a) is present in all three samples, but is dominated by ages between 133.7 and 104.9 Ma (*n*: 15), with a Late Cretaceous to earliest Paleocene component (*n*: 5) only evident in a single sample. Overall the population of Upper Unit white mica ^{40}Ar/^{39}Ar ages yields the greatest dispersion within individual samples 259.3 m.y., 226.6 m.y., and 68.5 m.y. Elimination of three outliers drastically reduces much of this dispersion (20.9 m.y., 9.5 m.y., and 68.5 m.y.).

Total fusion white mica ^{40}Ar/^{39}Ar analyses of 89 single grains from 13 Middle Unit samples yielded ages ranging from 52.1 ± 0.6 Ma to 11.8 ± 0.1 Ma. The dispersion within individual samples ranges from 38.1 m.y. to 1.9 m.y. Removal of two outliers (52.1 ± 0.6 Ma, 32.7 ± 0.5 Ma) yields middle Oligocene to middle Miocene ages (*n*: 81) ranging from 31.4 ± 0.9 Ma to 11.8 ± 0.1 Ma (Figures 8b and 8d). Mica ages from marbles typically range from 25 to 16 Ma; sample HY16 possesses a younger age population extending to 11.8 ± 0.1 Ma (Figure 8b). Middle Unit schist single-grain ages are from 23.6 ± 0.1 to 14.0 ± 0.3 Ma; these schists typically have slightly larger errors and a greater degree of age dispersion than most marble samples (Figure 8b). Sparse early Oligocene single grain analyses concentrated in HY07 and HY08 may define an early Oligocene age population (32.7 ± 0.5 Ma to 27.9 ± 1.1 Ma, *n*: 4) within the highest levels of the Middle Unit close to the upper detachment (Figures 8b and 8c). No uniform grain size control on white mica ages was observed in these analyses. Some samples exhibited both more tightly defined chemical compositions and age ranges (e.g., HY18), but this trend is not evident for most samples, which may suggest that white mica composition has an unpredictable control on age dispersion in these samples.

^{40}Ar/^{39}Ar analysis of 63 single grains from nine Lower Unit samples yielded ages ranging from 23.1 ± 0.2 Ma to 9.8 ± 0.1 Ma with a single 78.1 ± 0.3 Ma outlier (Figure 8c). Removal of the single outlier reduces the range of intrasample dispersion to 6.5–1.7 m.y. and Lower Unit ^{40}Ar/^{39}Ar white mica ages define two populations (i) An early-to-middle Miocene 3.1–3.5 Si phengitic population in marbles ranging from 23.1 ± 0.2 Ma to 15.5 ± 0.2 Ma; and (ii) a middle-to-late Miocene phengitic-to-muscovitic population in mica and calc-mica schists that ranges from 13.5 ± 0.1 Ma to 9.8 ± 0.1 Ma and 3.0–3.3 Si (Figures 8d and 7d) with a dominant population at ca. 12 Ma. Sample HY31 is from a higher structural level, has a greater proportion of calcite, and spans a range from 17.7 ± 0.6 Ma to 12.4 ± 0.2 Ma.

Though there are a range of grain sizes and ages in Middle and Lower unit marbles, there is no obvious grain size control on age. Mylonitic marbles with 50–100 µm long grains produce statistically identical ages to samples with mica great of sizes up to 500 µm. Plotting ^{39}Ar as a proxy for grain size against age shows no uniform relationship (Figure S6).

4.7. Zircon (U-Th)/He Geochronology

Zircon (U-Th)/He analysis was conducted on up to ten grains per sample for 21 zircon-bearing samples from Hymittos in order to elucidate the low-temperature (<200°C) geologic history of the massif. Weighted

average ages are reported for samples where dispersion is low and age ranges for samples where dispersion is high (2σ; Figure 8; Table S4).

Upper Unit zircon (U-Th)/He analysis (single crystals n: 44) from six samples of metasiliciclastic rocks yielded widely dispersed ages. Typically, zircons are euhedral with tabular to elongate habits and range from 220 to 100 μm in length; rarer subhedral and anhedral grains are stubby to equant and may lack one or both terminations. Crystals contained minimal inclusions and exhibited a range of metamictization. The dispersion comprises dates from late Oligocene to Late Cretaceous from five samples (27.9–72.2 Ma; n: 31; Figure 8a). A second, more dispersed Late to Early Cretaceous age population is present in sample HY01 (76.2–127.3 Ma; Figure 8a).

Zircon from the Middle Unit range in size from 110 to 50 μm and are commonly subrounded to rounded, clear, and colorless to rosy and translucent with stubby to tabular habits. Zircon (U-Th)/He analyses from 12 samples (n: 74) identified a middle and a late Miocene population (Figures 8b and 8d). The middle Miocene population (15.4 ± 1.0 Ma, n: 10) is observed in two samples: a cataclased quartz-feldspar-white mica ultramylonitic schist and a cataclased serpentinite melange located within the upper detachment brittle fault zone (Figure S1). A dominant population of late Miocene ages is recorded in samples from structurally deeper levels (n: 56, 12.0 ± 0.31 to 6.5 ± 0.2 Ma; Figures 8b and 8d). Eight spurious analyses were discarded due to low He, low U, or the presence of inclusions combined with anomalous ages (Table S4).

Lower Unit zircon from Cheroma Unit quartzite are typically subhedral and exhibit prismatic to tabular habits ranging in size from 380 to 105 μm. Grains from calc-schist and mica-schist range from 85 to 45 μm. Zircon (U-Th)/He analysis of Lower Unit samples HY35 (8.3 ± 1.0 Ma, n: 8), HY36 (8.5 ± 0.7 Ma, n: 5), and HY37 (7.9 ± 0.9 Ma, n: 10) produced late Miocene populations that are statistically identical (Figure 8e). Two anomalous analyses were discarded due to low U (Table S4).

5. Discussion

The significant differences in low-temperature geochronology, metamorphic grade, and degree of deformation between the Upper and Middle units support the conclusion that the upper detachment is a major tectonic contact. The detachment fault cross-cutting the massif displays consistent top-SSW kinematics, ductile-then-brittle deformation and is located along-strike of other exposures of the WCDS. The elongate north-south geomorphology of the massif (similar to exposures of other metamorphic domes within the western Cyclades; Figure 1b) presence of a major tectonic contact and low-angle detachment faults prove that Hymittos is a Cycladic-style metamorphic core complex. We suggest that the Upper Unit (Alepovouni Unit) is an exposure of the Pelagonian Zone, based on its lithologies, low metamorphic grade, age, and structural position overlying crystalline rocks of the Middle and Lower units. The presence of a cataclased serpentinite melange within the upper detachment is observed elsewhere in the Cyclades separating the Pelagonian and CBU (Selçuk Mèlange as reported in Okrusch & Bröcker, 1990; Ring & Layer, 2003). The footwall to the upper detachment (Middle and Lower units) are exposures of the LCBN evinced by the presence of a retrogressed blueschist facies mineral assemblage in metabasites of the Middle Unit and pelitic schists of the Middle and Lower units. To streamline the following discussion, we will consider the Middle and Lower units together as the Lower Plate; the Upper Unit and the overlying sedimentary basins are grouped into the Upper Plate.

The deformation of large blocks of rock is commonly heterogeneous and often diachronous (e.g., Chadwick, 1968), which complicates differentiating between different structural generations and correlating them across a region (Park, 1969). In geologic settings where deformation is relatively continuous (e.g., core complexes), structures that would traditionally be considered different generations may occur over geologically short time periods under the same conditions; this is termed progressive deformation (Tobisch & Paterson, 1988). In such a setting structures produced during the early portion of progressive deformation are frequently reoriented, refolded, cannibalized, and destroyed by the same conditions that created them producing composite structures (e.g., Grujic & Mancktelow, 1995; Platt & Berhmann, 1986; Turner & Weiss, 1963). We suggest that the ubiquitous overprinting of earlier structures by later generations is evidence that Hymittos underwent progressive deformation for >10 m.y. as indicated by the dispersion of ^{40}Ar/^{39}Ar ages (further discussed in section 5.2.3). As a result, we define folds and foliations that developed

under the sample principle stresses and uniformly affect all previous structures (F_{x-1}, F_{x-2}) as part of the same generation (F_x and S_x, respectively).

5.1. Upper Plate

The moderate upright folding, prevalence of N-S lineations, and cataclasite development in Upper Unit phyllites increases with proximity to the upper detachment. Calcite ribbons in calcitic rocks have been tentatively tied to intermediate strain at comparatively low temperature (Rybacki et al., 2003); likely all of these tectonic structures are a consequence of shallow crustal displacement along the detachment suggesting they correspond to the S_3 structures of the Middle and Lower units.

White mica within Upper Unit phyllites exhibit a range of grain sizes and morphologies, but overall show little evidence for ductile deformation or recrystallization (Figure 5a). Undulatory extinction is minimal, and the host rocks are low metamorphic grade. Taken together, these observations suggest that the white mica within Alepovouni phyllites have a detrital origin. White mica $^{40}Ar/^{39}Ar$ ages in the Upper Unit of Hymittos are more dispersed and significantly older than white mica from the Lower Plate (Figure 8). White mica ages from samples HY03 and HY05 are ca. 115 Ma similar to ca. 116 Ma $^{40}Ar/^{39}Ar$ ages reported from phengite ages of the Pelagonian Zone (Makrotantalon Unit) on Andros Island, although the Makrotantalon Unit ages are much less dispersed and reflect 116 Ma metamorphism (Huet et al., 2014). The ages from the Upper Unit are also similar to white mica ages from the Pelagonian Zone in the hanging wall of the Santorini Detachment System (Schneider et al., 2018). Some of the age dispersion in the Upper Unit samples may reflect thermal heating during widespread late Cretaceous metamorphism and plutonism within the Pelagonian Zone (Altherr et al., 1982; Bröcker & Franz, 2006; Patzak et al., 1994) or could represent partial resetting during stacking of the Upper Unit atop the CBU during the Eocene (Huyskens & Bröcker, 2014). Overall, we suggest these Cretaceous to early Paleocene $^{40}Ar/^{30}Ar$ ages represent a detrital white mica population that may have been partially reset during HP-LT Cretaceous metamorphism of the Pelagonian Zone (Lips et al., 1998; Maluski et al., 1981; Schermer et al., 1990).

Cretaceous to Eocene zircon (U-Th)/He ages preserved in the Upper Unit metasedimentary rocks of Hymittos are interpreted as a partially reset detrital age signature based on the dispersion of the analyses (Figure 8a). We suggest this partial resetting occurred during the low-grade metamorphism of the Upper Unit during which temperatures did not significantly exceed ~130°C (lower limit of the ZHe partial retention zone; Reiners & Brandon, 2006) as this would have fully reset the zircon (U-Th)/He systematics.

The majority of the Upper Unit has been eroded from atop the massif (Figures 2 and 3) and the late Miocene to Pleistocene terrestrial sedimentary rocks of the Athens and Mesogea basins contain clasts with a sub-Pelagonian Zone source and ZHe ages of 38–92 Ma (Krohe et al., 2010; Seman, 2016; Figure S2), indicating the Upper Unit was exposed and eroding during the Miocene. Presuming the partially reset ages reflect burial temperatures of ~130°C, it would be necessary to remove ~5–8 km of material (based on an estimated 25°C/km geothermal gradient) between the Eocene and the present. A sample of unmetamorphosed Athens Schist (HY02) overlying the Pelagonian rocks of Hymittos produced zircon (U-Th)/He ages indistinguishable from analyses of Alepovouni Unit samples (Figure 8a). Paleontology suggests the Athens Schists are Maastrichtian to Paleocene in age (Papanikolaou, Lozios, et al., 2004). We suggest that partially reset Paleocene to Eocene recorded in ZHe ages in Upper Unit reflects shallow burial and a short residence time in the partial retention zone. Consequently, we envisage a scenario where the material from the Upper Unit was eroded during the Miocene to Pliocene, which led to deposition of Pelagonian-derived sediments in the Mesogea and Athens basins. Thus, the Athens Schist may be in part recycled components of the Pelagonian Zone. Erosional removal of the Alepovouni Unit was perhaps driven by upward flexure of the metamorphic dome in the late Miocene.

5.2. Lower Plate

Our reinterpretation of the tectonostratigraphy of Hymittos differs from previous works (e.g., Krohe et al., 2010; Lekkas & Lozios, 2000; Lepsius, 1893; Marinos & Petraschek, 1956), which interpreted the dolomitic rocks in the northern massif as a graben and proposed a succession based on primary sedimentary layering of calcareous and siliciclastic sediments. The km-scale folding (F_2) within the Middle Unit was hitherto unrecognized and explains previously unresolved field observations including s- and z-fold orientations, inconsistent "stratigraphic" relationships, and contacts. Despite the complex structure, stretching and

mineral lineations are dominantly NNE-SSW, and kinematics are dominantly top-S. We suggest that this is due to reorientation of S_1 and S_2 foliation surfaces and lineations during top-S shear associated with the development of the S_3 foliation.

5.2.1. High-Pressure Metamorphism

Mineralogy and mineral chemistry indicate relics of a high-pressure assemblage that was pervasively overprinted during greenschist facies metamorphism in the Lower Plate. High-pressure metamorphism (M_1) is evident from relict glaucophane uncommonly observed in Kaissariani metabasic schists (Figure 5d). Chloritoid in thin section typically appears metastable, retrogressing to white mica and chlorite (Figure 5i). The stability field for chloritoid in Fe- and Al-rich metapelites overlaps with the stability field for glaucophane in metabasites (El-Shazly & Liou, 1991; Spear & Cheney, 1989). Due to the commonly observed intergrowth of chloritoid, white mica, and chlorite indicating retrogression, we suggest chloritoid growth occurred during M_1 metamorphism (Vidal et al., 1994). The absence of metabasic rocks within the Lower Unit of the massif prevents the unequivocal identification of more characteristic blueschist facies metamorphic assemblages.

White mica is used as both a thermobarometer and geochronometer because the mineral possesses a range of chemical composition strongly controlled by pressure and temperature (Parra et al., 2002; Vidal & Parra, 2000) and because of its elevated K content (McDougall & Harrison, 1999). When applied as a geobarometer, higher Si content has been correlated with elevated pressure (Massonne & Schreyer, 1987). Thus, the phengitic chemical compositions observed in marbles (Figures 7b and 7d) and the phengitic cores of zoned white mica in Kaissariani and Cheroma schists (Figure S2) are also compatible with a high-pressure metamorphic stage. This agrees with previous white mica-chlorite thermobarometry within the massif that identified a high-pressure metamorphic event in the Kaissariani schist ($300 \pm 25°C$, 1.4 ± 0.05 GPa; Baziotis et al., 2019).

5.2.2. Greenschist Facies Metamorphism

High-Si phengitic mica have been partially chemically re-equilibrated to moderate-Si phengite and muscovitic compositions (Figures 7a and 7b), which we suggest occurred along the retrograde path of M_1 metamorphism at and below upper greenschist facies conditions of $470 \pm 20°C$ and 0.8 ± 0.1 GPa for the Middle Unit (M_2; Baziotis, Proyer, et al., 2019). The new metamorphic conditions are further evinced by the muscovitic (Si-poor) rims on phengite-cored white mica crystals, zoned intergrowth of muscovitic and phengitic mica, growth of albite porphyroblasts, and the ubiquity of metamorphic chlorite and epidote. The thermal increase may be a result of higher heat flow relating to the emplacement of the metamorphic core complex (e.g., Roche et al., 2018).

Regrettably, there are currently no P-T estimates for the Lower Unit of Hymittos. We suggest that M_2 greenschist facies metamorphism was as hot (or slightly hotter) and associated deformation was more pervasive in the Lower Unit than in the Middle Unit based on the greater degree of compositional re-equilibration of white mica to a muscovitic composition (Figures 7a, 7b, 7c, and 7d), complete resetting of $^{40}Ar/^{39}Ar$ systematics (Figure 8c), and the presence of ductilely deformed Lower Unit dolomite; Middle Unit dolomite is exclusively brittlely deformed. The trend of lower tectonostratigraphic units having relatively higher grade metamorphism concurs with geothermobarometry on the LCBN from the Penteli Mountains and Lavrion elsewhere on Attica (Baziotis et al., 2009; Baziotis, Mposkos, et al., 2019; Scheffer et al., 2016).

5.2.3. Thermal and Deformation Induced Resetting of $^{40}Ar/^{39}Ar$ Systematics

High-pressure metamorphism in the Cyclades occurred in the Eocene, yet white mica $^{40}Ar/^{39}Ar$ analyses on phengitic mica from Hymittos do not produce Eocene ages. The minor population of middle to early Oligocene white mica $^{40}Ar/^{39}Ar$ ages in Middle Unit schists that overlap with 33–21 Ma Rb-Sr phengite ages from Evia (Ring et al., 2007) and 36–22 Ma white mica $^{40}Ar/^{39}Ar$ ages from the middle unit of Lavrion (Coleman et al., 2019) may correspond to diachronous Oligocene ca. 30 Ma greenschist facies overprinting (Cao et al., 2018; Huet et al., 2014), the last gasp of blueschist facies metamorphism during syn-orogenic exhumation (Cliff et al., 2017; Laurent et al., 2017; Peillod et al., 2017; Ring, Will, et al., 2007). Alternatively, the ages are reflective of partial resetting of an original ca. 50–40 Ma phengitic population produced during M_1 high-pressure metamorphism (Bröcker et al., 2004; Schneider et al., 2011). High-Si (>3.45; Bröcker et al., 2004) phengitic chemical compositions do not make up a major proportions of the Lower Plate analyses (Figures 7b and 7d), which may also explain the scarcity of early to middle Oligocene ages (Figures 8b, 8c, 8d, and 8e).

Peak temperatures during M_2 metamorphism ($470 \pm 20°C$; Baziotis, Proyer, et al., 2019) were sufficient to fully reset muscovite $^{40}Ar/^{39}Ar$ systematics (Figure 8b) but possibly not fully reset the high-Si phengite ages (Augier et al., 2005; Di Vincenzo et al., 2001; Laurent et al., 2017). That being said, the white mica $^{40}Ar/^{39}Ar$ ages in marbles occur over a relatively narrow age range (average intrasample dispersion is 4 m.y.) and show no obvious relationship to white mica composition so it is likely that $^{40}Ar/^{39}Ar$ systematics were reset even if temperature was not the dominant controlling factor. We suggest that white mica $^{40}Ar/^{39}Ar$ systematics were reset by latest Oligocene to early Miocene greenschist facies metamorphism as a consequence of (re) crystallization enhanced by fluid flow during syn-metamorphic deformation. Consequently, we suggest that the ca. 20 Ma peak in white mica $^{40}Ar/^{39}Ar$ ages (Figures 8d and 8e) is the timing of peak greenschist facies metamorphism for the Lower Plate rocks of Hymittos. The younger mid-Miocene ages in marbles may indicate minor muscovite (neo)crystallization on the retrograde path of M_2 metamorphism (Figures 8b and 8c).

White mica in Lower Plate marbles are typically subhedral to euhedral, relatively undeformed (Figures 5c and 5g) and preserve 25–16 Ma white mica $^{40}Ar/^{39}Ar$ ages with a distinct concentration at ca. 20 Ma (Figures 8b and 8c). The <10 m.y. range and subhedral to euhedral nature of the white mica in most Middle and Lower unit marbles suggests that were largely unaffected by progressive deformation at temperatures above 250°C, the lower limit for crystal-plastic deformation of calcite (Kennedy & White, 2001). The youngest marble white mica ages are middle Miocene. Hence, we interpret that white mica $^{40}Ar/^{39}Ar$ isotopic systems closed in both Middle and Lower unit marbles ca. 16 Ma. Ductile deformation of the marble mylonites likely ceased at temperatures close to 250°C where the calcitic marble mylonites would have significantly increased in strength and decreased in permeability (Kennedy & White, 2001), we suggest this prevented further recrystallization of white mica in marbles (Lewis et al., 1998).

White mica from Lower Plate schistose rocks have a variable muscovitic to moderate-Si phengitic composition (Figures 7a and 7b), chemical zonation, and exhibit a deformed appearance in thin section (Figure 5f). Compared to marble samples, Middle Unit schists show a greater dispersion of white mica $^{40}Ar/^{39}Ar$ ages ranging from early Oligocene to middle Miocene (Figure 8d). Schistose lithologies generally exhibit a greater sensitivity to changing P-T conditions than do marbles, which commonly avoid extensive re-equilibration due to differences in permeability, more stable mineralogy, and so forth (e.g., Ganor et al., 1989; Lewis et al., 1998; Lü et al., 2013). As the rocks of the Lower Plate cooled on the M_2 retrograde path, deformation would be preferentially accommodated by linked phyllosilicate layers. We speculate that the white mica $^{40}Ar/^{39}Ar$ ages from the Middle Unit schists record deformation-induced resetting of the latest Oligocene to early Miocene metamorphic population preserved in Middle Unit marbles. The greater age dispersion is a result of partial substitution and incomplete chemical re-equilibration observed in the mineral chemistry and chemical maps, as has been recognized in Lavrion and the Western Cyclades (Coleman et al., 2019; Cossette et al., 2015; Grasemann et al., 2012; Iglseder et al., 2011; Schneider et al., 2011). Lower Unit schistose rocks exhibit a smaller dispersion of white mica $^{40}Ar/^{39}Ar$ ages and compositions (Figure 7d) and are more pervasively deformed than equivalent samples from the Middle Unit. We suggest the majority of the white mica $^{40}Ar/^{39}Ar$ ages record complete recrystallization during pervasive ca. 12 Ma S_3 deformation along the lower detachment (HY32; HY33; HY34; Figure 8c). HY31 contains a significant proportion of calcite (Table S1), the sample occurs at a higher structural level, its mica are less sheared and deformed than other schistose samples (Figure 5i), and consequently mica $^{40}Ar/^{39}Ar$ ages are slightly older. We suggest HY31 was only partially reset during late Miocene deformation along the lower detachment. $^{40}Ar/^{39}Ar$ systematics have been fully reset in many Cheroma schist samples, yet the white mica compositions are dispersed, which suggests that S_3 deformation-induced recrystallization did not fully chemically re-equilibrate white mica compositions. This further supports the conclusion that the degree of dispersion of white mica chemistry does not have a clear control on age dispersion in these samples.

5.2.4. Onset of Brittle Deformation

Samples HY07 and HY08 preserve the oldest zircon (U-Th)/He ages (ca. 15 Ma) and white mica $^{40}Ar/^{39}Ar$ ages (early Oligocene) in the Lower Plate (Figures 8b and 8d). Furthermore, these are the only schistose samples to preserve $^{40}Ar/^{39}Ar$ ages that are uniformly older than ages from Middle Unit marbles. These samples are both located within the brittlely deformed fault zone of the upper detachment and are the structurally highest samples from within the Middle Unit. We suggest that these samples reflect preservation of a
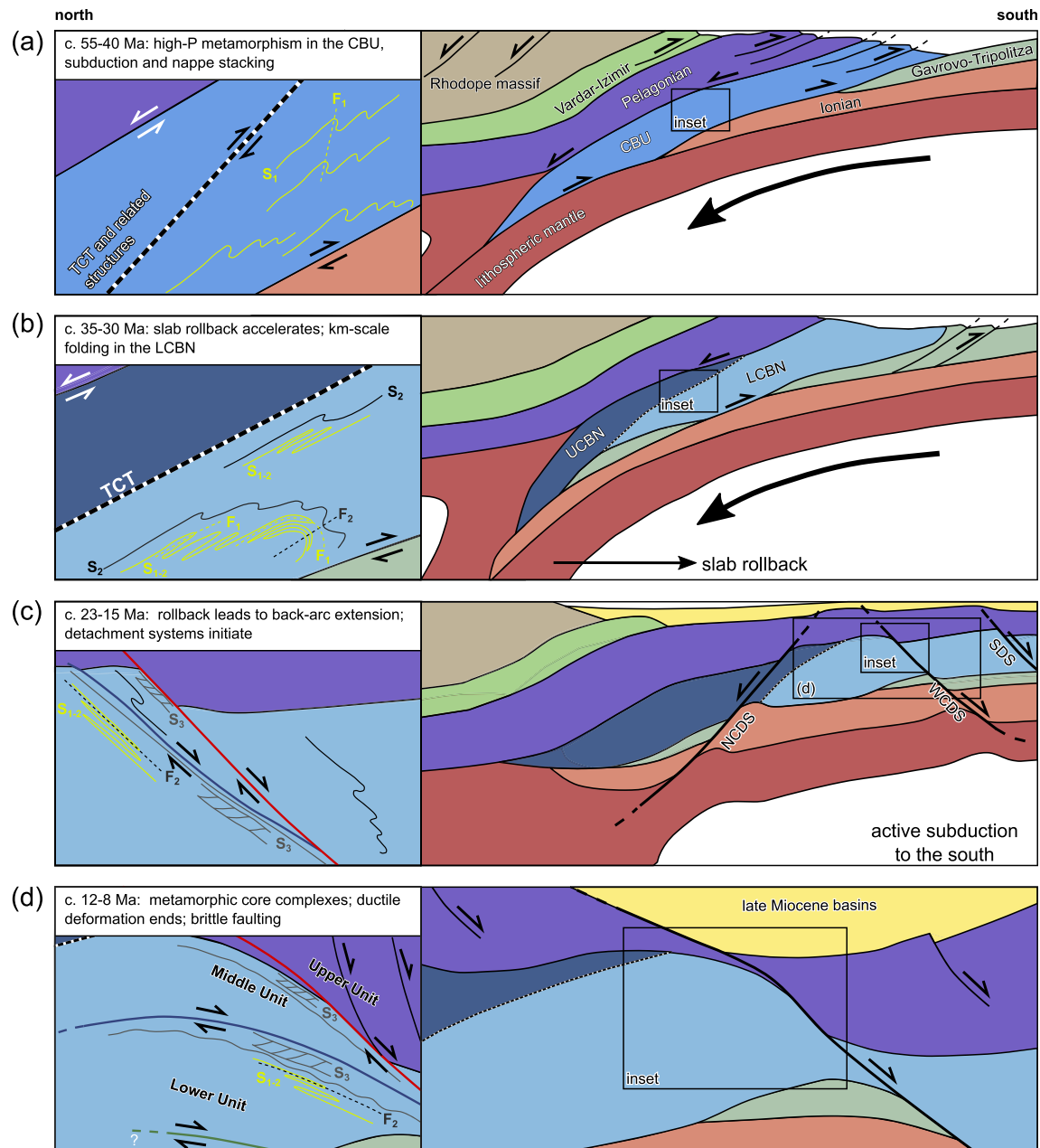
Figure 9. Unscaled, schematic diagram depicting the tectonic evolution of the proto-Aegean, Aegean and the units of the Hymittos massif. (a) At ca. 55-40 Ma: subduction and nappe-stacking produces high-P metamorphism in the CBU, coeval with the onset of synorogenic exhumation within the subduction channel. S_1 foliations and F_1 folds are produced by progressive deformation. (b) At ca. 35–30 Ma: slab rollback accelerates, and synorogenic exhumation juxtaposes the LCBN and UCBN along the Trans-Cycladic Thrust. S_2 foliations and F_2 folds form, reorienting and exploiting earlier structures. (c) At ca. 23–15 Ma: slab rollback has produced back-arc extension and crustal thinning, which initiated the detachment systems under greenschist facies conditions. Initial S_3 foliation develops, flattening and transposing older structures close to the detachments. Geochronology suggests the Hymittos detachments were coeval by the middle Miocene. (d) At ca. 12–8 Ma: metamorphic core complex development under waning greenschist facies conditions; the splays of the WCDS are an example of a horsetail structure accommodating the termination of a fault system as displacement approaches zero. Ductile deformation ceases on the Hymittos massif ca. 8 Ma transitioning to brittle faulting and the formation of the Mesogea and Athens basins overlying the Upper Unit.

structurally higher portion of the LCBN within the fault zone ca. 15 Ma even as the rest of the Lower Plate continued to exhume.

The dominant 10–8 Ma zircon (U-Th)/He ages in the Middle and Lower units of Hymittos are interpreted as reflecting relatively rapid cooling during late Miocene exhumation along the upper detachment. These data

exhibit a limited dispersion, and flat age-eU and age-ESR trends (Figures 8b, 8c, and S4), consistent with rapid cooling to temperatures below <130°C (Guenthner et al., 2013, 2014). The marked break in zircon (U-Th)/He cooling ages across the upper detachment suggests that this structure accommodated the majority of brittle, late Miocene deformation.

5.3. Tectonic History

By integrating a new bedrock map with quantitative data, a metamorphic and deformation history may be resolved for Hymittos. We propose M_1 was a HP-LT metamorphic event recorded in the Middle and Lower units of the massif evinced by high-Si phengite preserved in marbles, phengite-cored white mica in schists, relict glaucophane in metabasites, and chloritoid in Middle and Lower unit schists and calc-schists. Syn-metamorphic (M_1) deformation within the subduction channel produced the S_1 foliations preserved in albite porphyroblasts and quartz-rich microlithons and as highly attenuated or rootless isoclinal folds (Figures 5e and 9a). Baziotis, Proyer, et al. (2019) estimates the conditions of this metamorphic event at $300 \pm 25°C$, 1.4 ± 0.05 GPa based on chlorite-white mica thermobarometry. Eocene HP-LT metamorphism has been recognized regionally within the CBU (Altherr et al., 1979; Okrusch & Bröcker, 1990; Schneider et al., 2011; Tomaschek et al., 2003; Wijbrans & McDougall, 1986, 1988) and within the western Cyclades zircon U-Pb and white mica $^{40}Ar/^{39}Ar$ geochronology has documented ca. 40 Ma metamorphism on Serifos (Schneider et al., 2011).

HP-LT metamorphism was followed by or overlapped with roughly E-W compression and macroscopic folding of intercalated schist and marble layers producing the east-verging recumbent folds (F_2) of the Middle Unit (Figure 9b). We suggest this occurred during the Eocene to early Oligocene at mid-crustal depth within the subduction channel, possibly during basal thrusting that has been associated with the syn-orogenic exhumation of the CBU (Forster & Lister, 2009; Huet et al., 2009; Jolivet & Brun, 2010; Ring et al., 2010; Ring, Will, et al., 2007). Progressive shear reoriented and flattened perturbations in the S_1 foliation producing tight-to-isoclinal folds and the S_{1-2} foliation.

A pervasive greenschist facies (M_2) mineral assemblage in Middle and Lower unit rocks is recorded by muscovitic rims on zoned white mica, and the growth of chlorite, epidote, and albite porphyroblasts (Figure 5e). M_2 occurred during latest Oligocene to early Miocene coeval with exhumation of the Middle and Lower units through ductile top-SSW deformation along the detachments as recorded by white mica $^{40}Ar/^{39}Ar$ ages in Lower Plate marbles. The 25–16 Ma white mica $^{40}Ar/^{39}Ar$ ages are strikingly similar to regional ca. 25–18 Ma dates for the dominant greenschist facies metamorphism that has been correlated to post-orogenic extension-related exhumation throughout the Cyclades (e.g., Altherr et al., 1982; Bröcker et al., 1993; Bröcker et al., 2004; Bröcker & Franz, 1998; Wijbrans & McDougall, 1986, 1988; Wijbrans et al., 1990; Xypolias et al., 2012). We propose the M_2 greenschist facies metamorphic event on Hymittos is an expression of the widespread greenschist facies event, and the ages overlap with ca. 21–14 Ma white mica $^{40}Ar/^{39}Ar$ ages reported from Kea and Kythnos (Cossette et al., 2015; Grasemann et al., 2012; Iglseder et al., 2011) and 18–14 Ma from the Lower Unit of Lavrion (Coleman et al., 2019).

Progressive syn- to post-M_2 deformation likely produced the S_3 mylonitic foliation observed in the footwalls of the detachments (Figures 5e and 9c). This deformation also formed the open F_3 folds with N-S and E-W oriented hinges. White mica in Middle and Lower unit schists are aligned and stretched into the L_3 orientation suggesting the late Oligocene to Miocene white mica $^{40}Ar/^{39}Ar$ deformation ages are the product of recrystallization as a result of M_2-related syn-to-post-metamorphic deformation (Figures 8b and 8c). Continued accommodation of deformation within the schists led to shear and flattening of the F_2 folds into isoclines (Figure 6c). Sparse NE-SW and E-W oriented lineations in the Middle Unit (Figure 6f) may correspond to earlier deformation predating or during 50–40° clockwise rotation of the Aegean microplate during the latest Oligocene to mid-Miocene (van Hinsbergen et al., 2005).

During the late Miocene, as the Middle and Lower units cooled, ductile deformation was succeeded by brittle deformation along the detachments. Within the Middle and Lower units, deformation produced structurally controlled N-S aligned brittle slip lineations along S_3 and earlier foliations. This top-SSW ductile-then-brittle deformation along the detachment faults led to the exhumation of LCBN rocks as the footwall of an asymmetric metamorphic core complex producing extension parallel and perpendicular folding (F_3; Figure 9d). Similar fold styles are commonly observed in other crustal-scale detachment faults (e.g., Aravadinou &

Xypolias, 2017; Braathen et al., 2000; Fletcher & Bartley, 1994; Mancktelow & Pavlis, 1994); however, the extension perpendicular F_3 folds suggest the conditions of deformation on Hymittos require further investigation. During the latest stages of extension, the massif was dissected up by east-west trending high-angle normal faults and dextral and sinistral strike slip faults.

5.4. Northwestern Termination of the West Cycladic Detachment System

It has been previously observed that low-temperature geochronology is very consistent along-strike of the WCDS (Coleman et al., 2019). We suggest that these new data, along with the SSW-directed kinematics, conclusively demonstrate that the detachments of Hymittos are exposures of the WCDS that were ductilely active in the early and middle Miocene before transitioning to a wholly brittle structure at ca. 8–9 Ma represented by zircon (U-Th)/He cooling ages from Hymittos, Lavrion, Kea, Kythnos, and Serifos (Berger et al., 2013; Grasemann et al., 2012; Seman, 2016). The overlap between Middle Unit zircon (U-Th)/He ages (15–9 Ma) and Lower Unit white mica $^{40}Ar/^{39}Ar$ ages (ca. 12 Ma) suggests the lower detachment was ductilely deforming even as the upper detachment was brittlely active. Furthermore, the 15 Ma zircon cooling ages provide a minimum bound for the onset brittle faulting related to the WCDS on Hymittos.

Most Hymittos Middle Unit samples have similar white mica $^{40}Ar/^{39}Ar$ ages (23–15 Ma) compared to the lower tectonostratigraphic unit of Lavrion (18–14 Ma; Coleman et al., 2019). The only samples from Hymittos that have a similar age pattern to the middle unit of Lavrion are samples from the structurally highest levels of the Middle Unit of Hymittos (HY07, HY08; Figure 8b; Berger et al., 2013; Coleman et al., 2019; Seman, 2016). These samples are structurally higher portions of the CBU preserved in the detachment during faulting. Therefore, the lower and upper detachments of Lavrion may laterally join the upper detachment of Hymittos as a pair of splays.

The detachment systems of the Cyclades juxtapose CBU (LCBN and UCBN) footwalls against Pelagonian Zone hanging wall. To the west of Hymittos, the Pelagonian Zone is the dominant geological unit (Figures 1a and 1b). The absence of CBU to the west suggests the detachments of Hymittos have accommodated less displacement than detachments on islands closer to the center of the WCDS (i.e., Kea and Kythnos; Grasemann et al., 2012) and represent exposures of the lateral terminus of a Cycladic-style detachment. The late Miocene white mica $^{40}Ar/^{39}Ar$ ages, and their similarity to ages from the lower detachment of Serifos indicate that ductile deformation at the two ends of the fault was occurring simultaneously, suggesting a ductile shear zone ~150 km in lateral extent, terminating a comparatively short distance northwest of Hymittos and southeast of Serifos.

The significant difference in metamorphic grade and white mica $^{40}Ar/^{39}Ar$ and zircon (U-Th)/He ages between the Upper and Middle units of Hymittos, as well as the evidence that the Lower Unit of the massif experienced somewhat higher temperature conditions suggests that displacement along the Hymittos detachments must be significant. Thus, the WCDS may carry on several km to the northwest beneath the rocks of the Pelagonian Zone on the Greek mainland (Figure 1) possibly continuing along structures recently identified via gravimetry measurements (Dilalos et al., 2019). Top-NNE kinematics have been reported for the Pelagonian Zone in this region, possibly pointing to a terminus or linkage of the NCDS and WCDS (Diamantopoulos et al., 2009). The displacement gradients at the terminations of the structure must be extremely high, since the significant offset at Hymittos must be negligible within tens of kilometers to the northwest. This may in part be accommodated by the multi-plane detachments of Hymittos as a vertically oriented horsetail, serving the same mechanically necessary purpose as the horizontally oriented structures that are sometimes recognized as the termini of strike-slip faults (Kim & Sanderson, 2006).

5.5. Cycladic-Style Detachment Systems

The architecture and evolution of the detachment systems accommodating extension within the Cyclades are still debated. Multi-plane detachments are commonly associated with extension-triggered plutonism; in this model extension along a detachment fault produces crustal thinning, the rise of asthenosphere, and melting of the lower crust (Liati et al., 2009; Lister & Davis, 1989). The melt rises before being arrested at the brittle-ductile transition; in so doing, it deactivates the original fault and thermally weakens the crust above the pluton, leading to localization of a new detachment plane that accommodates subsequent deformation (Rabillard et al., 2018). Granitoid crystallization ages from along the WCDS are similar ca. 12–9 Ma for Serifos (Altherr et al., 1982; Iglseder et al., 2009) and Lavrion ca. 9–8 Ma (Liati et al., 2009). These

localities both expose multiple fault planes correlated to the WCDS, with youngest white mica $^{40}Ar/^{39}Ar$ ages suggesting the detachment branches that localized at the roof of these plutons were active at ca. 10 Ma (Berger et al., 2013; Coleman et al., 2019; Grasemann et al., 2012; Iglseder et al., 2009; Schneider et al., 2011). This has been interpreted to indicate a sequence of fault deactivation and relocalization in these and other localities (Tinos, Mykonos, and Ikaria; Brichau et al., 2010; Laurent et al., 2015; Beaudoin et al., 2015; Rabillard et al., 2018). Where plutons are not present, detachments exhibit a single plane (i.e., Kea, Kythnos, Sifnos, Andros; Iglseder et al., 2011; Ring et al., 2011; Grasemann et al., 2012; Huet et al., 2014).

On Hymittos, multiple faults of the WCDS are observed without spatially associated plutonism. Local studies on mineralization and airborne gravimetry to characterize the subsurface of Athens found no evidence for a magmatic body (Dilalos et al., 2019; Stouraiti et al., 2019). The late Miocene white mica ages in the Cheroma schists overlap with the oldest portions of the late Miocene zircon (U-Th)/He ages in both the Middle and Lower units (Figures 8b, 8c, 8d, and 8e). The lower detachment was ductilely deforming in the late Miocene as the upper detachment was brittlely deforming. Thus, another case for Cycladic-style detachments must be considered: Multi-plane detachments within the Cyclades may be co-active, and plutonism cannot be the only mechanism driving (re)localization.

In a regional context, the NE-vergent NCDS initiated before the SW-vergent WCDS: 35–30 Ma and 26–22 Ma, respectively (Grasemann et al., 2012; Jolivet et al., 2010). Rb-Sr and $^{40}Ar/^{39}Ar$ constrain the latest ductile deformation along the NCDS to 20–18 Ma (Laurent et al., 2017). The youngest ages related to ductile deformation on Hymittos are ca. 12 Ma, which is 6 m.y. younger than ca. 18 Ma ages of ductile deformation from Kea and Kythnos (Cossette et al., 2015; Grasemann et al., 2012) and are similar to 13–9 Ma white mica $^{40}Ar/^{39}Ar$ dates from a ductile-brittle branch of the WCDS on Serifos (Grasemann et al., 2012) and 14–10 Ma dates from the lower unit of Lavrion (Coleman et al., 2019). Thus, the WCDS continued to be active as a ductile structure ca. 8 m.y. after the NCDS began deforming brittlely. This suggests that extension within the Cyclades is diachronous and migrated southwards through time, agreeing with similar observations for the greater Aegean (Jolivet et al., 2003).

6. Conclusion

Bedrock mapping, white mica $^{40}Ar/^{39}Ar$ and zircon (U-Th)/He ages, and petrographic and structural analysis suggest the detachments of Hymittos are an extension of the Western Cycladic Detachment System (Figure 1b). The Upper Unit is part of the Pelagonian Zone, and regional evidence and zircon (U-Th)/He data suggest the Upper Unit exhumed during Eocene to recent erosion. The Middle and Lower units of Hymittos are correlated to the LCBN of the Cyclades. Our work suggests a series of deformation and metamorphic events: M_1 high-pressure low-temperature metamorphism and associated deformation correlated to Eocene metamorphism recognized elsewhere within the Cyclades. Foliations associated with this syn-orogenic deformation are transposed and refolded as an S_{1-2} foliation during west-verging folding. M_2 greenschist facies metamorphism occurred during the late Oligocene to early Miocene as indicated by white mica $^{40}Ar/^{39}Ar$ ages in Middle and Lower unit marbles. Middle to late Miocene ductile deformation partially to fully transposed S_{1-2} foliations into an S_3 transposition foliation and reset $^{40}Ar/^{39}Ar$ systematics in Middle and Lower unit schists. Finally, zircon (U-Th)/He cooling ages suggest the Middle and Lower units were exhuming under brittle conditions ca. 8 Ma. Field evidence and the overlap in deformation ages suggest that the upper and lower detachments were coeval in the middle Miocene. Co-active multi-plane detachments suggest a new endmember for Cycladic-style detachment systems.

Data Availability Statement

Datasets, additional figures, and a detailed methodology for this research are archived in the Mendeley Data repository: https://doi.org/10.17632/5vxzptg5gz.1.

References

Altherr, R., Kreuzer, H., Wendt, I., Lenz, H., Wagner, G. A., Keller, J., et al. (1982). A late Oligocene/early Miocene high temperature belt in the Attic-Cycladic crystalline complex (SE Pelagonian, Greece). *Geologisches Jahrbuch*, *23*, 97–164.
Altherr, R., Kreuzer, H., Wendt, I., Lenz, H., Wendt, I., Harre, W., & Dürr, S. (1994). Further evidence for a late Cretaceous low-pressure high-temperature terrane in the Cyclades, Greece. *Chemie der Erde*, *54*, 319–328.

Altherr, R., Schliestedt, M., Okrusch, M., Seidel, E., Kreuzer, H., Harre, W., et al. (1979). Geochronology of high-pressure rocks on Sifnos (Cyclades, Greece). *Contributions to Mineralogy and Petrology*, *70*, 245–255. https://doi.org/10.1007/bf00375354

Aravadinou, E., & Xypolias, P. (2017). Evolution of a passive crustal-scale detachment (Syros, Aegean region): Insights from structural and petrofabric analyses in the hanging-wall. *Journal of Structural Geology*, *103*, 57–74. https://doi.org/10.1016/j.jsg.2017.09.008

Aubouin, J. (1959). Contribution à l' étude géologique de la Grèce septentrionale: Les confins de l' Epire et de la Thessalie. *Annales Géologiques des Pays Helléniques*, *10*, 525.

Augier, R., Agard, P., Monié, P., Jolivet, L., Robin, C., & Booth-Rhea, G. (2005). Exhumation, doming and slab retreat in the Betic Cordillera (SE Spain): in situ $^{40}Ar/^{39}Ar$ ages and P-T-d-t paths for the Nevado-Filabride complex. *Journal of Metamorphic Geology*, *23*, 357–381. https://doi.org/10.1111/j.1525-1314.2005.00581.x

Augier, R., Jolivet, L., Gadenne, L., Lahfid, A., & Driussi, O. (2015). Exhumation kinematics of the Cycladic Blueschists Unit and back-arc extension, insight from the Southern Cyclades (Sikinos and Folegandros Islands, Greece). *Tectonics*, *34*, 152–185. https://doi.org/10.1002/2014TC003664

Baziotis, I., & Mposkos, E. (2011). Origin of metabasites from upper tectonic unit of the Lavrion area (SE Attica Greece): Geochemical implications for dual origin with distinct provenance of blueschist and greenschist's protoliths. *Lithos*, *126*, 161–173. https://doi.org/10.1016/j.lithos.2011.07.014

Baziotis, I., Mposkos, E., Windley, B. F., & Lamont, T. N. (2019). Exhumation of Attica high-pressure rocks in a subduction channel: New metamorphic PT constraints from Attica, NW Cyclades, Greece. *Lithos*, 105266. https://doi.org/10.1016/j.lithos.2019.105266

Baziotis, I., Proyer, A., & Mposkos, E. (2009). High-pressure/low-temperature metamorphism of metabasites in Lavrion area (SE Attica Greece): Implications for the preservation of peak metamorphic assemblages in blueschists and greenschists. *European Journal of Mineralogy*, *21*, 133–148. https://doi.org/10.1127/0935-1221/2008/0020-1853

Baziotis, I., Proyer, A., Mposkos, E., Windley, B., & Boukouvala, I. (2019). Exhumation of the high-pressure northwestern Cyclades, Aegean: New PT constraints, and geodynamic evolution. *Lithos*, *324-325*, 439–453. https://doi.org/10.1016/j.lithos.2018.11.027

Beaudoin, A., Augier, R., Laurent, V., Jolivet, L., Lahfid, A., Bosse, V., et al. (2015). The Ikaria high-temperature Metamorphic Core Complex (Cyclades, Greece): Geometry, kinematics and thermal structure. *Journal of Geodynamics*, *92*, 18–41. https://doi.org/10.1016/j.jog.2015.09.004

Berger, A., Schneider, D. A., Grasemann, B., & Stockli, D. (2013). Footwall mineralization during Late Miocene extension along the West Cycladic Detachment System, Lavrion Greece. *Terra Nova*, *25*, 181–191. https://doi.org/10.1111/ter.12016

Bonneau, M. (1984). Correlation of the Hellenide nappes in the south-east Aegean and their tectonic reconstruction. In J. E. Dixon & A. H. F. Robertson (Eds.), *The geological evolution of the Eastern Mediterranean, Geological Society of London Special Publication* (Vol. 17, pp. 517–527). London: Geological Society of London. https://doi.org/10.1144/GSL.SP.1984.017.01.38

Bonneau, M., & Kienast, J. R. (1982). Subduction, collision et schistes bleus: exemple de l'Egée, Grece. *Bulletin de la Societe Geologique de France*, *7*, 785–791. https://doi.org/10.2113/gssgfbull.s7-xxiv.4.785

Braathen, A., Nordgulen, Ø., Osmundsen, P. T., Andersen, T. B., Solli, A., & Roberts, D. (2000). Devonian, orogen-parallel, opposed extension of the Central Norway Caledonides. *Geology*, *28*, 615–618. https://doi.org/10.1130/0091-7613(2000)028<0615:dopoei>2.3.co;2

Brichau, S., Ring, U., Carter, A., Moni, P., Bolhar, R., Stockli, D., & Brunel, M. (2007). Extensional faulting on Tinos Island, Aegean Sea, Greece: How many detachments? *Tectonics*, *26*, TC4009. https://doi.org/10.1029/2006TC001969

Brichau, S., Thomson, S., & Ring, U. (2010). Thermochronometric constraints on the evolution of the Serifos detachment, Aegean Sea, Greece. *International Journal of Earth Sciences*, *99*(2), 279–393. https://doi.org/10.1007/s00531-008-0386-0

Bröcker, M., Bieling, D., Hacker, B., & Gans, P. (2004). High Si phengite records the time of greenschist-facies overprinting: Implications for models suggesting mega-detachments in the Aegean Sea. *Journal of Metamorphic Geology*, *22*, 427–442. https://doi.org/10.1111/j.1525-1314.2004.00524.x

Bröcker, M., & Franz, L. (1998). Rb-Sr isotope studies on Tinos Island (Cyclades, Greece): additional time constraints for metamorphism, extent of infiltration-controlled overprinting and deformational activity. *Geological Magazine*, *135*, 369–382. https://doi.org/10.1017/s0016756898008681

Bröcker, M., & Franz, L. (2006). Dating metamorphism and tectonic juxtaposition on Andros Island (Cyclades, Greece): Results of a Rb-Sr study. *Geological Magazine*, *143*, 609–620. https://doi.org/10.1017/s001675680600241x

Bröcker, M., Kreuzer, H., Matthews, A., & Okrusch, M. (1993). $^{40}Ar/^{39}Ar$ and oxygen isotope studies of polymetamorphism from Tinos Island, Cycladic blueschist belt, Greece. *Journal of Metamorphic Geology*, *11*, 223–240. https://doi.org/10.1111/j.1525-1314.1993.tb00144.x

Brun, J.-P., & Faccenna, C. (2008). Exhumation of high- pressure rocks driven by slab rollback. *Earth and Planetary Science Letters*, *272*(1–2), 1–7. https://doi.org/10.1016/j.epsl.2008.02.038

Brunn, J. H. (1956). Contribution à l'étude géologique du Pinde septentrional et de la Macédoine occidentale. *Annales Géologiques des Pays Helléniques*, *7*, 358.

Buick, I. (1991). Mylonitic fabric development on Naxos. *Journal of Structural Geology*, *13*, 643–655. https://doi.org/10.1016/0191-8141(91)90027-g

Cao, S., Neubauer, F., Bernroider, M., & Genser, J. (2018). Eocene high-pressure metamorphism and Oligocene retrogression on Naxos, Cyclades, Greece: Significance for Aegean tectonics and $^{40}Ar/^{39}Ar$ dating in polyphase metamorphic rocks. *Tectonophysics*, *745*, 66–94. https://doi.org/10.1016/j.tecto.2018.08.009

Cardozo, N., & Allmendinger, R. W. (2013). Spherical projections with OSXStereonet. *Computers & Geosciences*, *51*, 193–205. https://doi.org/10.1016/j.cageo.2012.07.021

Chadwick, B. (1968). Deformation and metamorphism in the Lukmanier region, central Switzerland. *Bulletin of the Geological Society of America*, *79*, 1123–1150. https://doi.org/10.1130/0016-7606(1968)79[1123:damitl]2.0.co;2

Chatzaras, V., Dorr, W., Finger, F., Xypolias, P., & Zulauf, G. (2013). U-Pb single zircon ages and geochemistry of metagranitoid rocks in the Cycladic Blueschists (Evia Island): Implications for the Triassic tectonic setting of Greece. *Tectonophysics*, *595–596*, 125–139. https://doi.org/10.1016/j.tecto.2012.05.016

Clement, B. (1976). Essai d'interpretation structurale d'un secteur des zones internes Helléniques: l' Attique-Beotie. *Bulletin de la Société Géologique de France*, *2*, 309–316. https://doi.org/10.2113/gssgfbull.S7-XVIII.2.309

Cliff, R. A., Bond, C. E., Butler, R. W. H., & Dixon, J. E. (2017). Geochronological challenges posed by continuously developing tectono-metamorphic systems: Insights from Rb-Sr mica ages from the Cycladic Blueschist Belt, Syros (Greece). *Journal of Metamorphic Geology*, *35*, 197–211. https://doi.org/10.1111/jmg.12228

Coleman, M. (2020). Coleman_2020_Tectonics. *Mendeley Data, V1*. https://doi.org/10.17632/5vxzptg5gz.1

Coleman, M., Dubosq, R., Schneider, D. A., Grasemann, B., & Soukis, K. (2019). Along-strike consistency of an extensional detachment system. *Terra Nova*, *31*(3), 220–223. https://doi.org/10.1111/ter.12388

Cossette, E., Schneider, D. A., Warren, C. J., & Grasemann, B. (2015). Lithological, rheological, and fluid infiltration control on $^{40}Ar/^{39}Ar$ ages in polydeformed rocks from the West Cycladic detachment system, Greece. *Lithosphere*, *7*, 189–205. https://doi.org/10.1130/l416.1

Cowie, P. A., & Scholz, C. H. (1992). Physical explanation for the displacement-length relationship for faults using a post-yield fracture mechanics model. *Journal of Structural Geology*, *14*, 1133–1148. https://doi.org/10.1016/0191-8141(92)90065-5

Di Vincenzo, G., Ghiribelli, B., Giorgetti, G., & Palmeri, R. (2001). Evidence of a close link between petrology and isotope records: constraints from SEM, EMP, TEM and in situ $^{40}Ar-^{39}Ar$ laser analyses on multiple generations of white micas (Lanterman Range, Antarctica). *Earth and Planetary Science Letters*, *192*, 389–405. https://doi.org/10.1016/s0012-821x(01)00454-x

Diamantopoulos, A., Krohe, A., & Mposkos, E. (2009). Kinematics of conjugate shear zones, displacement partitioning and fragmentation of the upper rigid crust during denudation of high-P rocks (Pelagonian and Sub-Pelagonian Zones, Greece). *Tectonophysics*, *473*, 84–98. https://doi.org/10.1016/j.tecto.2008.05.028

Dilalos, S., Alexopoulos, J. D., & Lozios, S. (2019). New insights on subsurface geological and tectonic structure of the Athens basin (Greece), derived from urban gravity measurements. *Journal of Applied Geophysics*, *167*, 73–105. https://doi.org/10.1016/j.jappgeo.2019.04.024

Doutsos, T., Pe-Piper, G., Boronkay, K., & Koukouvelas, I. (1993). Kinematics of the Central Hellenides. *Tectonics*, *12*, 935–953. https://doi.org/10.1029/93TC00108

Dragovic, B., Baxter, E. F., & Caddick, M. J. (2015). Pulsed dehydration and garnet growth during subduction revealed by zoned garnet geochronology and thermodynamic modelling, Sifnos, Greece. *Earth and Planetary Science Letters*, *413*, 111–122. https://doi.org/10.1016/j.epsl.2014.12.024

Dürr, S., Altherr, R., Keller, J., Okrusch, M., & Seidel, E. (1978). The median Aegean crystalline belt: stratigraphy, structure, metamorphism, magmatism. In H. Closs, D. Roeder, & K. Schmidt (Eds.), *Alps, Apennines, Hellenides: Geodynamic investigation along geo-traverses by an international group of geoscientists, IUCG. Sci. Rep.* (Vol. 38, pp. 537–564). Stuttgart: Schweizerbart.

Elliott, D. (1976). A discussion on natural strain and geological structure—The energy balance and deformation mechanism of thrust sheets. *Philosophical Transactions of the Royal Society of London*, *283*, 289–312. https://doi.org/10.1098/rsta.1976.0086

El-Shazly, A. K., & Liou, J. G. (1991). Glaucophane chloritoid-bearing assemblages from NE Oman: Petrologic significance and a petrogenetic grid for high P metapelites. *Contributions to Mineralogy and Petrology*, *107*(2), 180–201. https://doi.org/10.1007/bf00310706

Faure, M., Bonneau, M., & Pons, J. (1991). Ductile deformation and syntectonic granite emplacement during the late Miocene extension of the Aegean (Greece). *Bulletin de la Société Géologique de France*, *5*(1), 3–11. https://doi.org/10.2113/gssgfbull.162.1.3

Flansburg, M. E., Stockli, D. F., Poulaki, E. M., & Soukis, K. (2019). Tectono-magmatic and stratigraphic evolution of the cycladic basement, Ios Island, Greece. *Tectonics*, *38*, 2291–2316. https://doi.org/10.1029/2018TC005436

Fletcher, J., & Bartley, J. M. (1994). Constrictional strain in a non-coaxial shear zone: Implications for fold and rock fabric development, central Mojave metamorphic core complex, California. *Journal of Structural Geology*, *16*(4), 555–570. https://doi.org/10.1016/0191-8141(94)90097-3

Forster, M. A., & Lister, G. S. (1999). Detachment faults in the Aegean core complex of Ios, Cyclades, Greece. In U. Ring, M. T. Brandon, G. S. Lister, & S. D. Willet (Eds.), *Exhumation processes: Normal faulting, ductile flow and erosion, Special Publications of the Geological Society* (Vol. 154, pp. 305–323). London: Continental Tectonics.

Forster, M. A., & Lister, G. S. (2005). Several distinct tectonometamorphic slices in the Cycladic eclogite-bluschist belt, Greece. *Contributions to Mineralogy and Petrology*, *150*, 523–545. https://doi.org/10.1007/s00410-005-0032-9

Forster, M. A., & Lister, G. S. (2009). Core-complex-related extension of the Aegean lithosphere intiated at the Eocene-Oligocene transition. *Journal of Geophysical Research*, *114*, B02401. https://doi.org/10.1029/2007jb005382

Fytikas, M., Innocenti, F., Manetti, P., Mazzuoli, R., Peccerillo, A., & Villari, L. (1984). Tertiary to Quaternary evolution of volcanism in the Aegean region. *Geological Society, London, Special Publications*, *17*, 689–699. https://doi.org/10.1144/gsl.sp.1984.017.01.55

Ganor, J., Matthews, A., & Paldor, N. (1989). Constraints on effective diffusivity during oxygen isotope exchange at a marble-schist contact, Sifnos (Cylcades), Greece. *Earth and Planetary Science Letters*, *94*(3–4), 208–216. https://doi.org/10.1016/0012-821x(89)90140-4

Gautier, P., & Brun, J.-P. (1994). Crustal-scale geometry and kinematics of late-orogenic extension in the central Aegean (Cyclades and Ewia Island). *Tectonophysics*, *238*(1–4), 399–424. https://doi:10.1016/0040-1951(94)90066-3

Gerogiannis, N., Xypolias, P., Chatzaras, V., Aravadinou, E., & Papavlou, K. (2019). Deformation within the Cycladic subduction-exhumation channel: New insights from the enigmatic Makrotantalo nappe (Andros, Aegean). *International Journal of Earth Sciences*, *108*, 817–843. https://doi.org/10.1007/s00531-019-01680-3

Grasemann, B., Huet, B., Schneider, D. A., Rice, A. H. N., Lemmonnier, N., & Tschegg, C. (2018). Miocene postorogenic extension of the Eocene synorogenic imbricated Hellenic subduction channel: New constraints from Milos (Cyclades, Greece). *Geological Society of America Bulletin*, *130*, 238–262. https://doi.org/10.1130/b31731.1

Grasemann, B., & Petrakakis, K. (2007). Evolution of the Serifos metamorphic core complex. *Journal of the Virtual Explorer*, *27*, 2. https://doi.org/10.3809/jvirtex.2007.00170

Grasemann, B., Schneider, D. A., Stockli, D. F., & Iglseder, C. (2012). Miocene bivergent crustal extension in the Aegean: Evidence from the western Cyclades (Greece). *Lithosphere*, *4*, 23–39. https://doi.org/10.1130/l164.1

Grujic, D., & Mancktelow, N. S. (1995). Folds with axes parallel to the extension direction: An experimental study. *Journal of Structural Geology*, *17*, 279–291. https://doi.org/10.1016/0191-8141(94)e0048-4

Guenthner, W. R., Reiners, P. W., Ketcham, R. A., Nasdala, L., & Giester, G. (2013). Helium diffusion in natural zircon: radiation damage, anisotropy, and the interpretation of zircon (U-Th)/He thermochronology. *American Journal of Science*, *313*, 145–198. https://doi.org/10.2475/03.2013.01

Guenthner, W. R., Reiners, P. W., & Tian, Y. (2014). Interpreting date-eU correlations in zircon (U-Th)/He datasets: A case study from the Longmen Shan, China. *Earth and Planetary Science Letters*, *403*, 328–339. https://doi.org/10.1016/j.epsl.2014.06.050

Huet, B., Labrousse, L., & Jolivet, L. (2009). Thrust or detachment? Exhumation processes in the Aegean: Insight from a field study on Ios (Cyclades, Greece). *Tectonics*, *28*, TC3007. https://doi:10.1029/2008TC002397

Huet, B., Labrousse, L., Monié, P., Malvoisin, B., & Jolivet, L. (2014). Coupled phengite $^{40}Ar-^{39}Ar$ geochronology and thermobarometry: P-T-t evolution of Andros Island (Cyclades, Greece). *Geological Magazine*, *152*(4), 711–727. https://doi.org/10.1017/S0016756814000661

Huyskens, M. H., & Bröcker, M. (2014). The status of the Makrotantalon Unit (Andros, Greece) within the structural framework of the Attic-Cycladic Crystalline Belt. *Geological Magazine*, *151*(3), 430–446. https://doi.org/10.1017/S0016756813000307

Iglseder, C., Grasemann, B., Rice, A. H. N., Petrakakis, K., & Schneider, D. A. (2011). Miocene south-directed low-angle normal fault evolution on Kea (West Cycladic detachment system, Greece). *Tectonics*, *30*, TC4013. https://doi.org/10.1029/2010TC002802

Iglseder, C., Grasemann, B., Schneider, D. A., Petrakakis, K., Miller, C., Klötzli, U. S., et al. (2009). I- and S-type plutonism on Serifos (W-Cyclades, Greece). *Tectonophysics*, *473*, 69–83. https://doi:10.1016/j.tecto.2008.09.021

Jacobshagen, V. (1986). *Geologie von Griechenland* (pp. 1–363). West Berlin: Gebrueder Borntraeger.

Jolivet, L., & Brun, J.-P. (2010). Cenozoic geodynamic evolution of the Aegean. *International Journal of Earth Sciences*, *99*(1), 109–138. https://doi.org/10.1007/s00531-008-0366-4

Jolivet, L., & Faccenna, C. (2000). Mediterranean extension and the Africa-Aurasia collision. *Tectonics*, *19*(6), 1095–1106. https://doi.org/10.1029/2000TC900018

Jolivet, L., Faccenna, C., Goffé, B., Burov, E., & Agard, P. (2003). Subduction tectonics and exhumation of high-pressure metamorphic rocks in the Mediterranean orogens. *American Journal of Science*, *303*(5), 353–409. https://doi.org/10.2475/ajs.303.5.353

Jolivet, L., Lecomte, E., Huet, B., Denèle, Y., Lacombe, O., Labrousse, L., et al. (2010). The north cycladic detachment system. *Earth and Planetary Science Letters*, *289*, 87–104. https://doi.org/10.1016/j.epsl.2009.10.032

Jolivet, L., Menant, A., Sternai, P., Rabillard, A., Arbaret, L., Augier, R., et al. (2015). The geological signature of a slab tear below the Aegean. *Tectonophysics*, *659*, 166–182. https://doi.org/10.1016/j.tecto.2015.08.004

Jolivet, L., & Patriat, M. (1999). Ductile extension and the formation of the Aegean Sea. In B. Durand, L. Jolivet, F. Horváth, & M. Séranne (Eds.), *The Mediterranean Basins: Tertiary extension within the Alpine orogen*, *Special Publications of the Geological Society* (Vol. 156, pp. 427–456). London: The Geological Society.

Katsiavrias, N., Solakius, N., & Salaj, J. (1991). The age of the Agios Konstantinos limestone at Lavrion, southeastern Attica, Greece. *Geologica Carpathica*, *42*, 303–309.

Keiter, M., Ballhaus, C., & Tomaschek, F. (2011). *A new geological map of the Island of Syros (Aegean Sea, Greece): Implications for lithostratigraphy and structural history of the Cycladic Blueschist Unit*, Geological Society of America.

Kennedy, L. A., & White, J. C. (2001). Low-temperature recrystallization in calcite: Mechanisms and consequences. *Geology*, *29*, 1027–1030. https://doi.org/10.1130/0091-7613(2001)029<1027:ltricm>2.0.co;2

Kim, Y., & Sanderson, D. J. (2006). Structural similarity and variety at the tips in a wide range of strike-slip faults: A review. *Terra Nova*, *18*, 330–344. https://doi.org/10.1111/j.1365-3121.2006.00697.x

Krohe, A., Mposkos, E., Diamantopoulos, A., & Kaouras, G. (2010). Formation of basins and mountain ranges in Attica (Greece): The role of Miocene to Recent low-angle normal detachment faults. *Earth-Science Reviews*, *98*, 81–104. https://doi.org/10.1016/j.earscirev.2009.10.005

Lagos, M., Scherer, E. E., Tomaschek, F., Münker, C., Keiter, M., Berndt, J., & Ballhaus, C. (2007). High precision Lu-Hf geochronology of Eocene eclogite-facies rocks from Syros, Cyclades, Greece. *Chemical Geology*, *243*(1–2), 16–35. https://doi.org/10.1016/j.chemgeo.2007.04.008

Latsoudas, C. (2003). *Geological map of Greece, scale 1:50,000, "Koropi-Plaka" sheet*. Athens: publication of the Institute of Geology & Mineral Exploration.

Laurent, V., Beaudoin, A., Jolivet, L., Arbaret, L., Augier, R., Rabillard, A., & Menant, A. (2015). Interrelations between extensional shear zones and synkinematic intrusions: The example of Ikaria Island (NE Cyclades, Greece). *Tectonophysics*, *651–652*, 152–171. https://doi.org/10.1016/j.tecto.2015.03.020

Laurent, V., Huet, B., Labrousse, L., Jolivet, L., Monié, P., & Augier, R. (2017). Extraneous argon in high-pressure metamorphic rocks: Distribution, origin and transport in the Cycladic Blueschist Unit (Greece). *Lithos*, *272–273*, 315–335. https://doi.org/10.1016/j.lithos.2016.12.013

Laurent, V., Jolivet, L., Roche, V., Augier, R., Scaillet, S., & Cardello, G. L. (2016). Strain localization in a fossilized subduction channel: Insights from the Cycladic Blueschist Unit (Syros, Greece). *Tectonophysics*, *672–673*, 150–169. https://doi:10.1016/j.tecto.2016.01.036

Lekkas, S., & Lozios, S. (2000). Tectonic structure of Mt. Hymittos. *Annales Géologiques des Pays Helléniques*, *38*, 47–62.

Lekkas, S., Skourtsos, E., Soukis, K., Kranis, H., Lozios, S., Alexopoulos, A., & Koutsovitsis, P. (2011). *Late Miocene detachment faulting and crustal extension in SE Attica (Greece)*. Vienna, Austria: European Geosciences Union General Assembly.

Leleu, M., & Neumann, M. (1969). Age of Attic formations (Greece): From Palaeozoic to Mesozoic. *Comptes Rendus Hebdomadaires des Seances de l'Académie des Sciences Série D*, *268*, 1361–1363.

Lepsius, R. (1893). *Geologie von Attika* (Vol. 4, p. 592). Berlin: Zeitsch. F. Praktische Geologie.

Lewis, S., Holness, M., & Graham, C. (1998). Ion microprobe study of marble from Naxos, Greece: Grain-scale fluid pathways and stable isotope equilibration during metamorphism. *Geology*, *26*(10), 935–938. https://doi.org/10.1130/0091-7613(1998)026<0935:imsomf>2.3.co;2

Liati, A., Skarpelis, N., & Fanning, C. M. (2013). Late Permian-Early Triassic igneous activity in the Attic Cycladic Belt (Attica): New geochronological data and geodynamic implications. *Tectonophysics*, *595–596*, 140–147. https://doi.org/10.1016/j.tecto.2012.05.009

Liati, A., Skarpelis, N., & Pe-piper, G. (2009). Late Miocene magmatic activity in the Attic-Cycladic belt of the Aegean (Lavrion Se Attica Greece): Implications for the geodynamic evolution and timing of ore deposition. *Geological Magazine*, *146*, 732–742. https://doi.org/10.1017/s0016756809006438

Lips, A. L. W., White, S. H., & Wijbrans, J. R. (1998). ^{40}Ar/^{39}Ar laserprobe direct dating of discrete deformational events: A continuous record of early Alpine tectonics in the Pelagonian Zone, NW Aegean area, Greece. *Tectonophysics*, *298*, 133–153. https://doi.org/10.1016/s0040-1951(98)00181-4

Lister, G. S., Banga, G., & Feenstra, A. (1984). Metamorphic core complexes of Cordilleran type in the Cyclades, Aegean Sea, Greece. *Geology*, *12*, 221–225. https://doi.org/10.1130/0091-7613(1984)12<221:mccoct>2.0.co;2

Lister, G. S., & Davis, G. A. (1989). The origin of metamorphic core complexes and detachment faults formed during Tertiary continental extension in the northern Colorado River region, U.S.A. *Journal of Structural Geology*, *11*(1-2), 65–94. https://doi.org/10.1016/0191-8141(89)90036-9

Lister, G. S., & Forster, M. A. (2016). White mica ^{40}Ar/^{39}Ar age spectra and the timing of multiple episodes of high-P mineral growth in the Cycladic eclogite-blueschist belt, Syros, Aegean Sea, Greece. *Journal of Metamorphic Geology*, *34*, 401–421. https://doi.org/10.1111/jmg.12178

Lozios, S., Soukis, K., & Antoniou, V. (2019). A guide to lithostratigraphy and structural inventory of the Cycladic Blueschist Unit rocks of NE Attica (Greece). *Journal of the Virtual Explorer, Electronic Edition*, 1441–8142. https://doi.org/10.3809/jvirtex.2016.08691

Lü, Z., Bucher, K., & Lifei, Z. (2013). Omphacite-bearing calcite marble and associated coesite-bearing pelitic schist from the meta-ophiolitic belt of Chinese western Tianshan. *Jounral of Asian Earth Sciences*, *76*, 37–47. https://doi.org/10.1016/j.jseaes.2013.07.034

Maluski, H., Bonneau, M., & Kienast, J. R. (1987). Dating the metamorphic events in the Cycladic area: ^{39}Ar/^{40}Ar data from metamorphic rocks of the island of Syros (Greece). *Bulletin de la Société Géologique de France*, *8*, 833–842. https://doi.org/10.2113/gssgfbull.iii.5.833

Maluski, H., Vergely, P., Bavay, D., Bavay, P., & Katsikatsos, G. (1981). ^{40}Ar/^{39}Ar dating of glaucophanes and phengites in southern Euboa (Greece), geodynamic implications. *Bulletin de la Société Géologique de France*, *5*, 469–476. https://doi.org/10.2113/gssgfbull.s7-xxiii.5.469

Mancktelow, N. S., & Pavlis, T. L. (1994). Fold-fault relationships in low-angle detachment systems. *Tectonics*, *13*(3), 668–685. https://doi.org/10.1029/93TC03489

Marinos, G., & Petraschek, W. (1956). *Lavrion*. Athens: Institute of Geology and Underground Research.

Marinos, G., & Symeonidis, N. (1974). Neue Funde aus Pikermi (Attika, Griechenland) und eine allgemeine geologische Übersicht des paläontologischen Raumes. *Annales Géologiques des Pays Helléniques*, *XXVI*, 1–20.

Martel, S. J. (1997). Effects of cohesive zones on small faults and implications for secondary fracturing and fault trace geometry. *Journal of Structural Geology*, *19*, 835–847. https://doi.org/10.1016/s0191-8141(97)00002-3

Massonne, H.-J., & Schreyer, W. (1987). Phengite geobarometry based on the limiting assemblage with K-feldspar, phlogopite and quartz. *Contributions to Mineralogy and Petrology*, *96*(2), 212–224. https://doi.org/10.1007/bf00375235

McDougall, I., & Harrison, T. M. (1999). *Geochronology and thermochronology by the ^{40}Ar/^{39}Ar method*. Oxford University Press.

Mehl, C., Jolivet, L., & Lacombe, O. (2005). From ductile to brittle: Evolution and localization of deformation below a crustal detachment (Tinos, Cyclades, Greece). *Tectonics*, *24*, TC4017. https://doi.org/10.1029/2004TC001767

Mehl, C., Jolivet, L., Lacombe, O., Labrousse, L., & Rimmele, G. (2007). Structural evolution of Andros (Cyclades, Greece): A key to the behaviour of a (flat) detachment with an extending continental crust. In T. Taymaz, Y. Yilmaz, & Y. Dilek (Eds.), *The Geodynamics of the Aegean and Anatolia*, *Special Publications of the Geological Society* (Vol. 291, pp. 41–73). London: The Geological Society.

Négris, P., & Meunier, S. (1915). *Roches cristallophylliennes et tectonique de la Grèce*. Athens: Imprimerie P. D. Sakellarios.

Okrusch, M., & Bröcker, M. (1990). Eclogites associated with high-grade blueschists in the Cyclades archipelago, Greece: A review. *European Journal of Mineralogy*, *2*, 451–478. https://doi.org/10.1127/ejm/2/4/0451

Papanikolaou, D. (1984). The three metamorphic belts of the Hellenides: A review and a kinematic interpretation. In J. E. Dixon & A. H. F. Roberston (Eds.), *The geological evolution of the Eastern Mediterranean*, *Geological Society of London Special Publication* (Vol. 17, pp. 551–561).

Papanikolaou, D. (1987). Tectonic evolution of the Cycladic blueschist belt (Aegean Sea, Greece). In H. H. Helgeson (Ed.), *Chemical transport in metasomatic processes* (pp. 429–450). Dordrecht. Netherlands: Springer.

Papanikolaou, D. (2009). Timing of tectonic emplacement of the ophiolites and terrane paleogeography in the Hellenides. *Lithos*, *108*, 262–280. https://doi.org/10.1016/j.lithos.2008.08.003

Papanikolaou, D., Bassi, E.-K., Kranis, C., & Danamos, G. (2004). Paleogeographic evolution of the Athens basin from Late Miocene up to present. *Bulletin of the Geological Society of Greece*, *XXXVI*, 816–825. https://doi.org/10.12681/bgsg.16822

Papanikolaou, D., Lozios, S., Soukis, S., & Skourtsos, E. (2004). The geological structure of the "Athens Schists" allochthon system. *Bulletin of the Geological Society of Greece*, *36*, 1550–1559. https://doi.org/10.12681/bgsg.16513

Papanikolaou, D., & Papanikolaou, I. (2007). Geological, geomorphological and tectonic structure of the NE Attica and seismic hazard implications for the northern edge of the Athens plain. *Bulletin of the Geological Society of Greece*, *XXXX*, 425–438. https://doi.org/10.12681/bgsg.16634

Papanikolaou, D., & Royden, L. H. (2007). Disruption of the Hellenic arc: Late Miocene extensional detachment faults and steep Pliocene–Quaternary normal faults—or what happened at Corinth? *Tectonics*, *26*, TC5003. https://doi.org/10.1029/2006TC002007TC5003

Park, R. G. (1969). Structural correlation in metamorphic belts. *Tectonophysics*, *7*, 323–338. https://doi.org/10.1016/0040-1951(69)90077-8

Parra, T., Vidal, O., & Jolivet, L. (2002). Relation between deformation and retrogression in blueschist metapelites of Tinos island (Greece) evidenced by chlorite-mica local equilibria. *Lithos*, *63*, 41–66. https://doi.org/10.1016/s0024-4937(02)00115-9

Patzak, M., Okrusch, M., & Kreuzer, H. (1994). The Akrotiri Unit of the island of Tinos, Cyclades, Greece: Witness to a lost terrane of Late Cretaceous age. *Neues Jahrbuch für Geologie und Paläontologie Abhandlungen*, *194*, 211–252.

Peillod, A., Ring, U., Glodny, J., & Skelton, A. (2017). An Eocene/Oligocene blueschist-/greenschist facies P-T loop from the Cycladic Blueschist Unit on Naxos Island, Greece: Deformation-related re-equilibration vs. thermal relaxation. *Journal of Metamorphic Geology*, *35*, 805–830. https://doi.org/10.1111/jmg.12256

Photiades, A., & Carras, N. (2001). Stratigraphy and geological structure of the Lavrion area (Attica Greece). *Bulletin of the Geological Society of Greece*, *34*, 103–109. https://doi.org/10.12681/bgsg.16949

Photiades, A., & Saccani, E. (2006). Geochemistry and tectonomagmatic significance of the HP/LT metaophiolites of the Attic-Cycladic zone in the Lavrion area (Attica Greece). *Ofioliti*, *31*, 89–102.

Platt, J. P., & Berhmann, J. H. (1986). Structures and fabrics in a crustal-scale shear zone, Betic Cordillera, SE Spain. *Journal of Structural Geology*, *8*, 15–33. https://doi.org/10.1016/0191-8141(86)90014-3

Poulaki, E. M., Stockli, D. F., Flansburg, M. E., & Soukis, K. (2019). Zircon U-Pb chronostratigraphy and provenance of the cycladic blueschist unit and the nature of the contact with the cycladic basement on Sikinos and Ios Islands, Greece. *Tectonics*, *38*(10), 3586–3613. https://doi.org/10.1029/2018TC005403

Rabillard, A., Arbaret, L., Jolivet, L., Le Breton, N., Gumiaux, C., Augier, R., & Grasemann, B. (2015). Interactions between plutonism and detachments during metamorphic core complex formation, Serifos Island (Cyclades, Greece). *Tectonics*, *34*, 1080–1106. https://doi.org/10.1002/2014TC003650

Rabillard, A., Jolivet, L., Arbaret, L., Bessiere, E., Laurent, V., Menant, A., et al. (2018). Synextensional granitoids and detachment systems within Cycladic metamorphic core complexes (Aegean Sea, Greece): Toward a regional tectonomagmatic model. *Tectonics*, *37*, 2328–2362. https://doi.org/10.1029/2017TC004697

Reinecke, T., Altherr, R., Hartung, B., Hatzipanagiotou, K., Kreuzer, H., Harre, W., et al. (1982). Remnants of a Late Cretaceous high temperature belt on the island of Anafi (Cyclades, Greece). *Neues Jahrbuch fur Mineralogie, Abhandlungen*, *145*, 157–182.

Reiners, P. W., & Brandon, M. T. (2006). Using thermochronology to understand orogenic erosion. *Annual Review of Earth and Planetary Sciences*, *34*, 419–466. https://doi.org/10.1146/annurev.earth.34.031405.125202

Reischmann, T. (1998). Pre-Alpine origin of tectonic units from the metamorphic complex of Naxos, Greece, identified by single zircon Pb/Pb dating. *Bulletin of the Geological Society of Greece*, *32*, 101–111.

Rieder, M., Cavazzini, G., D'Yakonov, Y. S., Frank-Kamenetskii, V. A., Gottardi, G., Guggenheim, S., et al. (1998). Nomenclature of the micas. *The Canadian Mineralogist*, *36*, 41–48.

Ring, U., Glodny, J., Will, T., & Thomson, S. (2007). An Oligocene extrusion wedge of blueschist-facies nappes on Evia, Aegean Sea, Greece: Implications for the early exhumation of high-pressure rocks. *Journal of the Geological Society of London*, *164*, 637–652. https://doi.org/10.1144/0016-76492006-041

Ring, U., Glodny, J., Will, T., & Thomson, S. (2010). The Hellenic subduction system: High-pressure metamorphism, exhumation, normal faulting, and large-scale extension. *Annual Review of Earth and Planetary Sciences*, *38*(1), 45–76. https://doi.org/10.1146/annurev.earth.050708.170910

Ring, U., Glodny, J., Will, T. M., & Thomson, S. (2011). Normal faulting on Sifnos and the South Cycladic Detachment System, Aegean Sea, Greece. *Journal of the Geological Society, London*, *168*, 751–768. https://doi.org/10.1144/0016%76492010-76492064

Ring, U., & Layer, P. W. (2003). High-pressure metamorphism in the Aegean, eastern Mediterranean: Underplating and exhumation from the Late Cretaceous until the Miocene to recent above the retreating Hellenic subduction zone. *Tectonics*, *22*(3), 1022. https://doi.org/10.1029/2001TC001350

Ring, U., Will, T., Glodny, J., Kumerics, C., Gessner, K., Thomson, S., et al. (2007). Early exhumation of high-pressure rocks in extrusion wedges: Cycladic Blueschist Unit in the eastern Aegean, Greece, and Turkey. *Tectonics*, *26*, TC2001. https://doi.org/10.1029/2005TC001872

Robertson, S. (1999). BGS rock classification scheme volume 2: Classification of metamorphic rocks. In *British Geological Survey Research Report*.

Roche, V., Laurent, V., Cardello, G. L., Jolivet, L., & Scaillet, S. (2016). Anatomy of the Cycladic Blueschist Unit on Sifnos Island (Cyclades, Greece). *Journal of Geodynamics*, *97*, 62–87. https://doi.org/10.1016/j.jog.2016.03.008

Roche, V., Sternai, P., Guillou-Frottier, L., Menant, A., Jolivet, L., Bouchot, V., & Gerya, T. (2018). Emplacement of metamorphic core complexes and associated geothermal systems controlled by slab dynamics. *Earth and Planetary Science Letters*, *483*, 322–333. https://doi.org/10.1016/j.epsl.2018.06.043

Royden, L. H. (1993). The tectonic expression of slab pull at continental convergent boundaries. *Tectonics*, *12*(2), 303–325. https://doi.org/10.1029/92TC02248

Rybacki, E., Paterson, M. S., Wirth, R., & Dresen, G. (2003). Rheology of calcite-quartz aggregates deformed to large strain in torsion. *Journal of Geophysical Research*, *108*(2), 2089. https://doi.org/10.1029/2002jb001833

Scheffer, C., Vanderhaeghe, O., Lanari, P., Tarantola, A., Ponthus, L., Photiades, A., & France, L. (2016). Syn- to post-orogenic exhumation of metamorphic nappes: Structure and thermobarometry of the western Attic-Cycladic metamorphic complex (Lavrion, Greece). *Journal of Geodynamics*, *96*, 174–193. https://doi.org/10.1016/j.jog.2015.08.005

Schermer, E. R., Lux, D. R., & Burchfiel, B. C. (1990). Temperature-time history of subducted continental crust, Mount Olympos region, Greece. *Tectonics*, *9*, 1165–1195. https://doi.org/10.1029/TC009i005p01165

Schneider, D., Grasemann, B., Lion, A., Soukis, K., & Draganits, E. (2018). Geodynamic significance of the Santorini Detachment System (Cyclades, Greece). *Terra Nova*, *2018*, 1–9. https://doi.org/10.1111/ter.12357

Schneider, D. A., Senkowski, C., Vogel, H., Grasemann, B., & Iglseder, C. (2011). Eocene tectonometamorphism on Serifos (Western Cyclades) deduced from zircon depth-profiling geochronology and mica thermochronology. *Lithos*, *125*, 151–172. https://doi.org/10.1016/j.lithos.2011.02.005

Schöpfer, M. P. J., Childs, C., Manzocchi, T., & Walsh, J. J. (2017). Three-dimensional distinct element method modelling of the growth of normal faults in layered sequences. *Geological Society, London, Special Publications*, *439*(1), 307–332. https://doi.org/10.1144/sp439.17

Seman, S. (2016). *The tectonostratigraphy of the Cycladic Blueschist Unit and new garnet geo/thermochronology techniques* (PhD thesis). Austin: University of Texas at Austin.

Seman, S., Stockli, D. F., & Soukis, K. (2017). The provenance and internal structure of the Cycladic Blueschist Unit revealed by detrital zircon geochronology, Western Cyclades, Greece. *Tectonics*, *36*, 1407–1429. https://doi.org/10.1002/2016TC004378

Siivola, J., & Schmid, R. (2007). Recommendations by the IUGS subcommission on the systematics of metamorphic rocks: Web version 01.02.07, BGS. *British Geological Survey*.

Skourlis, K., & Doutsos, T. (2003). The Pindos fold-and-thrust belt (Greece): Inversion kinematics of a passive continental margin. *International Journal of Earth Sciences*, *92*, 891–903. https://doi.org/10.1007/s00531-003-0365-4

Soukis, K., & Stockli, D. F. (2013). Structural and thermochronometric evidence for multistage exhumation of southern Syros, Cycladic islands, Greece. *Tectonophysics*, *595–596*, 148–164. https://doi.org/10.1016/j.tecto.2012.05.017

Spear, F. S., & Cheney, J. T. (1989). A petrogenetic grid for pelitic schists in the system SiO_2-Al_2O_3-FeO-MgO-K_2O-H_2O. *Contributions to Mineralogy and Petrology*, *101*, 149–164. https://doi.org/10.1007/bf00375302

Stampfli, G. M., Vavassis, I., De Bono, A., Rosselet, F., Matti, B., & Bellini, M. (2003). Remnants of the Palaeotethys oceanic suture-zone in the western Tethyan area. *Bollettino della Societa Geologica Italiana e del Servizio Geologico d'Italia*, *2*, 1–23.

Stouraiti, C., Soukis, K., Voudouris, P., Mavrogonatos, C., Lozios, S., Lekkas, S., et al. (2019). Silver-rich sulfide mineralization in the northwestern termination of the Western Cycladic Detachment System, at Agios Ioannis Kynigos, Hymittos Mt. (Attica, Greece): A mineralogical, geochemical and stable isotope study. *Ore Geology Reviews*, *111*, 1–16. https://doi.org/10.1016/j.oregeorev.2019.102992

Tobisch, O. T., & Paterson, S. R. (1988). Analysis and interpretation of composite foliations in areas of progressive deformation. *Journal of Structural Geology*, *10*(7), 745–754. https://doi.org/10.1016/0191-8141(88)90081-8

Tomaschek, F., Kennedy, A. K., Villa, I. M., Lagos, M., & Ballhaus, C. (2003). Zircons from Syros, Cyclades, Greece—Recrystallization and mobilization of zircon during high-pressure metamorphism. *Journal of Petrology*, *44*, 1977–2002. https://doi.org/10.1093/petrology/egg067

Tschegg, C., & Grasemann, B. (2009). Deformation and alteration of a granodiorite during low-angle normal faulting (Serifos, Greece). *Lithosphere*, *1*(3), 139–154. https://doi.org/10.1130/l33.1

Turner, F. J., & Weiss, L. E. (1963). *Structural analysis of metamorphic tectonites* (pp. 1–545). New York: McGraw-Hill.

Urai, J., Schuiling, R., & Jansen, J. (1990). Alpine deformation on Naxos (Greece). In R. J. Knipe & E. H. Rutter (Eds.), *Deformation mechanisms, rheology and tectonics*, *Geological Society of London Special Publication* (Vol. 360, pp. 509–522). London: Geological Society of London.

Uunk, B., Brouwer, F., ter Voorde, M., & Wijbrans, J. (2018). Understanding phengite argon closure using single grain fusion age distributions in the Cycladic Blueschist Unit on Syros, Greece. *Earth and Planetary Science Letters*, *484*, 192–203. https://doi.org/10.1016/j.epsl.2017.12.031

van Hinsbergen, D. J. J., Langereis, C. G., & Meulenkamp, J. E. (2005). Revision of the timing, magnitude and distribution of Neogene rotations in the western Aegean region. *Tectonophysics*, *396*(1–2), 1–34. https://doi.org/10.1016/j.tecto.2004.10.001

Vidal, O., & Parra, T. (2000). Exhumation paths of high pressure metapelites obtained from local equilibria for chlorite-phengite assemblages. *Geology Magazine*, *35*, 139–161. https://doi.org/10.1002/gj.856

Vidal, O., Theye, T., & Chopin, C. (1994). Experimental study of chloritoid stability at high pressure and various fO_2 conditions. *Contributions to Mineralogy and Petrology*, *118*(3), 256–270. https://doi.org/10.1007/bf00306647

Wiesmayr, G., & Grasemann, B. (2005). Sense and non-sense of shear in flanking structures with layer-parallel shortening: Implications for fault-relates folds. *Journal of Structural Geology*, 27, 249–264. https://doi.org/10.1016/j.jsg.2004.09.001

Wijbrans, J. R., & McDougall, I. (1986). ^{40}Ar/^{39}Ar dating of white micas from an Alpine high-pressure metamorphic belt on Naxos (Greece): Resetting of the argon isotopic system. *Contributions to Mineralogy and Petrology*, 93, 187–194. https://doi.org/10.1007/bf00371320

Wijbrans, J. R., & McDougall, I. (1988). Metamorphic evolution of the Attic Cycladic Metamorphic Belt on Naxos (Cyclades, Greece) utilizing ^{40}Ar/^{39}Ar age spectrum measurements. *Journal of Metamorphic Geology*, 6, 571–594. https://doi.org/10.1111/j.1525-1314.1988.tb00441.x

Wijbrans, J. R., Schliestedt, M., & York, D. (1990). Single grain argon laser probe dating of phengites from the blueschist to greenschist transition on Sifnos (Cyclades, Greece). *Contributions to Mineralogy and Petrology*, 104, 582–593. https://doi.org/10.1007/bf00306666

Wind, S. C., Schneider, D. A., Hannington, M. D., & McFarlane, C. R. M. (2020). Regional similarities in lead isotopes and trace elements in galena of the Cyclades Mineral District, Greece with implications for the underlying basement. *Lithos*, 366–367, 1–27. https://doi.org/10.1016/j.lithos.2020.105559

Xypolias, P., Iliopoulos, I., Chatzaras, V., & Kokkalas, S. (2012). Subduction-and exhumation- related structures in the Cycladic Blueschists: Insights from south Evia Island (Aegean region, Greece). *Tectonics*, 31, TC2001. https://doi.org/10.1029/2011TC002946

Xypolias, P., Kokkalas, S., & Skourlis, K. (2003). Upward extrusion and subsequent transpression as a possible mechanism for the exhumation of HP/LT rocks in Evia island (Aegean Sea, Greece). *Journal of Geodynamics*, 35, 303–332. https://doi.org/10.1016/s0264-3707(02)00131-x

Zlatkin, O., Avigad, D., & Gerdes, A. (2018). New detrital zircon geochronology from the Cycladic Basement (Greece): Implications for the Paleozoic Accretion of Peri-Gondwanan Terranes to Laurussia. *Tectonics*, 37, 4679–4699. https://doi.org/10.1029/2018TC005046

References From the Supporting Information

Carslaw, H. S., & Jaeger, J. C. (1959). *Conduction of heat in solids*. Oxford: Clarendon Press.

Dazé, A., Lee, J. K. W., & Villeneuve, M. (2003). An intercalibration study of the Fish Canyon sanidine and biotite ^{40}Ar/^{39}Ar standards and some comments on the age of the Fish Canyon Tuff. *Chemical Geology*, 199, 111–127. https://doi.org/10.1016/s0009-2541(03)00079-2

Dodson, M. (1973). Closure temperature in cooling geochronological and petrological systems. *Contributions to Mineralogy and Petrology*, 40, 259–274. https://doi.org/10.1007/BF00373790

Ehlers, T. A. (2005). Crustal thermal processes and the interpretation of thermochronometer data. *Reviews in Mineralogy and Geochemistry*, 58(1), 315–350. https://doi.org/10.2138/rmg.2005.58.12

Farley, K. A., Shuster, D. L., Watson, E. B., Wanser, K. H., & Balco, G. (2010). Numerical investigations of apatite ^{4}He/^{3}He thermochronometry. *Geochemistry, Geophysics, Geosystems*, 11, Q10001. https://doi.org/10.1029/2010GC003243

Gautheron, C., & Tassan-Got, L. (2010). A Monte Carlo approach to diffusion applied to noble gas/helium thermochronology. *Chemical Geology*, 273(3–4), 212–224. https://doi.org/10.1016/j.chemgeo.2010.02.023

Guenthner, W. R., Reiners, P. W., DeCelles, P. G., & Kendall, J. (2015). Sevier belt exhumation in central Utah constrained from complex zircon (U-Th)/He data sets: Radiation damage and He inheritance effects on partially reset detrital zircons. *Geological Society of America Bulletin*, 127(3–4), 323–348. https://doi.org/10.1130/B31032.1

Gutiérrez-Alonso, G., Fernández-Suárez, J., Collins, A. S., Abad, I., & Nieto, F. (2005). Amazonian Mesoproterozoic basement in the core of the Ibero-Armorican Arc: ^{40}Ar/^{39}Ar detrital mica ages complement the zircon's tale. *Geology*, 33(8), 637. https://doi.org/10.1130/G21485.1

Harrison, M., Celerier, J., Aikman, A. B., Hermann, J., & Heizler, M. T. (2009). Diffusion of ^{40}Ar in muscovite. *Geochimica et Cosmochimica Acta*, 73, 1039–1050. https://doi.org/10.1016/j.gca.2008.09.038

Ketcham, R. A., Gautheron, C., & Tassan-Got, L. (2011). Accounting for long alpha-particle stopping distances in (U-Th-Sm)/He geochronology: Refinement of the baseline case. *Geochmica Et Cosmochimica Acta*, 75(24), 7779–7791. http://doi.org/10.1016/j.gca.2011.10.011

Kuiper, K. F., Deino, A., Hilgen, F. J., Krijgsman, W., Renne, P. R., & Wijbrans, J. R. (2008). Synchronizing rock clocks of earth history. *Science*, 320, 500–504. https://doi.org/10.1126/science.1154339

Lister, G. S., & Williams, P. F. (1979). Fabric development in shear zones: Theoretical controls and observed phenomena. *Journal of Structural Geology*, 1–4, 283–297. https://doi.org/10.1016/0191-8141(79)90003-8

Meesters, A., & Dunai, T. J. (2002). Solving the production-diffusion equation for finite diffusion domains of various shapes: Part 1. Implications for low-temperature (U-Th)/He thermochronology. *Chemical Geology*, 186(3–4), 333–344. https://doi.org/10.1016/S0009-2541(01)00422-3

Min, K., Mundil, R., Renne, P. R., & Ludwig, K. R. (2000). A test for systematic errors in ^{40}Ar/^{39}Ar geochronology through comparison with U/Pb analysis of a 1.1-Ga rhyolite. *Geochimica et Cosmochimica Acta*, 64, 73–98. https://doi.org/10.1016/s0016-7037(99)00204-5

Powell, J., Schneider, D., Stockli, D., & Fallas, K. (2016). Zircon (U-Th)/He thermochronology of Neoproterozoic strata from the Mackenzie Mountains, Canada: Implications for the Phanerozoic exhumation and deformation history of the northern Canadian Cordillera. *Tectonics*, 35, 663–689. https://doi.org/10.1002/2015TC003989

Reiners, P. W., Farley, K. A., & Hickes, H. (2002). He diffusion and (U–Th)/He thermochronometry of zircon: Initial results from Fish Canyon Tuff and Gold Butte. *Tectonophysics*, 349, 297–308. https://doi.org/10.1016/s0040-1951(02)00058-6

Reiners, P. W., Spell, T. L., Nicolescu, S., & Zanetti, K. A. (2004). Zircon (U-Th)/He thermochronometry: He diffusion and comparisons with ^{40}Ar/^{39}Ar dating. *Geochimica et Cosmochimica Acta*, 68(8), 1857–1887. https://doi.org/10.1016/j.gca.2003.10.021

Renne, P. R., & Norman, E. B. (2001). Determination of the half-life of ^{37}Ar by mass spectrometry. *Physical Review C: Nuclear Physics*, 63, 1–3. https://doi.org/10.1103/physrevc.63.047302

Renne, P. R., Swisher, C. C., Deino, A. L., Karner, D. B., Owens, T. L., & DePaolo, D. J. (1998). Intercalibration of standards, absolute ages and uncertainties in ^{40}Ar/^{39}Ar dating. *Chemical Geology*, 145, 117–152. https://doi.org/10.1016/s0009-2541(97)00159-9

Roddick, J. C. (1983). High precision intercalibration of ^{40}Ar-^{39}Ar standards. *Geochemica Cosmochimica Acta*, 47, 887–898. https://doi.org/10.1016/0016-7037(83)90154-0

Ross, J. (2019). *Pychron*. https://doi.org/10.5281/zenodo.9884

Steiger, R. H., & Jäger, E. (1977). Subcommission on geochronology: Convention on the use of decay constants in geo- and cosmochronology. *Earth and Planetary Science Letters*, 36, 359–362. https://doi.org/10.1016/0012-821x(77)90060-7

Warren, C. J., Hanke, F., & Kelley, S. P. (2012). When can muscovite ^{40}Ar/^{39}Ar dating constrain the timing of metamorphic exhumation? *Journal of Chemical Geology*, 291, 29–86. https://doi.org/10.1016/j.chemgeo.2011.09.017

Watson, E. B., Wanser, K. H., & Farley, K. A. (2010). Anisotropic diffusion in a finite cylinder, with geochemical applications. *Geochimica et Cosmochimica Acta*, *74*(2), 614–633. https://doi.org/10.1016/j.gca.2009.10.013

Wolfe, M. R., & Stockli, D. F. (2010). Zircon (U-Th)/He thermochronometry in the KTB drill hole, Germany, and its implications for bulk He diffusion kinetics in zircon. *Earth and Planetary Science Letters*, *295*(1–2), 69–82. https://doi.org/10.1016/j.epsl.2010.03.025